1 **The relation of wind-driven coastal and offshore upwelling in the Benguela Upwelling System**

2 Mohammad Hadi Bordbar*, Volker Mohrholz and Martin Schmidt

3 Leibniz Institute for Baltic Sea Research Warnemünde (IOW), Rostock, Germany

4 * Corresponding author, *Email address:* hadi.bordbar@io-warnemuende.de,

5 Ocean.Circulation@gmail.com

6 **Abstract**

7 Spatial and temporal variations of nutrient-rich upwelled water across the major eastern bound-

8 ary upwelling systems are primarily controlled by the surface wind with different, and sometimes

9 contrasting, impacts on coastal upwelling systems driven by alongshore wind and offshore

10 upwelling systems driven by the local wind-stress-curl. Here, concurrently measured wind-fields,

11 satellite-derived Chlorophyll-a concentration along with a state-of-the-art ocean model simula-

12 tion spanning 2008-2018 are used to investigate the connection between coastal and offshore

13 physical drivers of the Benguela Upwelling System (BUS). Our results indicate that the spatial

14 structure of long-term mean upwelling derived from Ekman theory and the numerical model are

15 fairly consistent across the entire BUS and closely followed by the Chlorophyll-a pattern. The var-

16 iability of the upwelling from the Ekman theory is proportionally diminished with offshore dis-

17 tance, whereas different and sometimes opposite structures are revealed in the model-derived

18 upwelling. Our result suggests the presence of sub-mesoscale activity (i.e., filaments and eddies)

19 across the entire BUS with a large modulating effect on the wind-stress-curl-driven upwelling off

20 Lüderitz and Walvis Bay. In Kunene and Cape Frio upwelling cells, located in the northern sector

21 of the BUS, the coastal upwelling and open-ocean upwelling frequently alternate each other,

22 whereas they are modulated by the annual cycle and mostly in phase off Walvis Bay. Such a phase

23 relationship appears to be strongly seasonally dependent off Lüderitz and across the southern

24 BUS. Thus, our findings suggest this relationship is far more complex than currently thought and

25 seems to be sensitive to climate changes with short- and far-reaching consequences for this vul-

26 nerable marine ecosystem.

1- Introduction

Similar to other major upwelling systems, any changes in the intensity and timing of upwelling and associated nutrient flux have different and sometimes contrasting impacts on the growth of individual phytoplankton size-classes across the Benguela Upwelling System (BUS; Rykaczewski et al., 2008; Lamont et al., 2019). In fact, this determines the regional diversity and population of the commercially valuable pelagic fishes (Rykaczewski et al., 2008). Given the increased observational evidence concerning natural and anthropogenic climate change across the BUS (Doney et al., 2012; Bachelery et al., 2016; Bonino et al, 2019), sensitivity of the local upwelling (e.g., timing, intensity, duration) to the regional surface atmospheric flow is of great ecological and socio-economic importance.

The BUS is characterized by distinctive features compared with other main eastern boundary upwelling systems (Fig. 1). It is identified with a perennial upwelling across its northern part and a strong seasonal cycle across the southern part which peaks between November and March (Bakun and Nelson 1991; Shannon and Nelson 1996; Duncombe Rae 2005; Lass and Mohrholz 2008; Junker et al., 2017). It is bounded both southward and northward by warm waters (Shannon and Nelson 1996; Hutchings et al. 2009; Bachelery et al., 2016; Lamont et al., 2019). In the southern flank across the southern tip of Africa (Fig.1), it meets warmer and saltier waters carried by the swift Agulhas Current with large variability in the form of sub-mesoscale eddies (Lass and Mohrholz 2008; Hutchings et al. 2009; Rubio et al., 2009; Bachelery et al., 2016). In the northern flank, it is bordered by warm and nutrient-enriched waters transported by the poleward Angola Current (Shannon, 1985; Hutchings et al. 2009; Bachelery et al., 2016; Koseki et al. 2019).

48 Ocean dynamics controls the strength of the upwelling which affects the availability of nutrients,

49 the primary production, and consequently the abundance and the diversity of pelagic fishes (Bar-

50 low et al., 2005; Lamont et al., 2019). Ekman transport driven by alongshore equator-ward winds

51 over the southwestern African coast pushes surface coastal waters offshore (Shannon, 1985; Lass

52 and Mohrholz, 2008). Near the coast, a narrow-band of upwelling forms which brings nutrient-

53 enriched water into the euphotic zone (Shannon, 1985; Fennel, 1999; Siegfried, et al., 2019). This

54 type of upwelling is known as Ekman coastal upwelling. Its fast vertical velocity favors large-cell

55 phytoplankton with high nutrient demands (Rykaszewski et al., 2008; Lamont et al., 2019). Given

56 the predator-prey body size relationship, the zooplankton communities are, thus, driven towards

57 large size species which primarily shapes the aquatic food web (Rykaczewski et al., 2008; Was-

58 mund et al., 2014; Lamont et al., 2019). Further offshore, the slow wind-stress-curl-driven (WSCD)

59 upwelling supports a lower rate of nutrient flux to the euphotic zone (Shannon 1985; Fennel 2007;

60 Mazzini et al., 2013; Jacox et al., 2018). This favors small-size species with enhanced surface-to-

61 volume ratio and high adaptability to nutrient-limited environments (Johnson, 1976; Hense and

62 Beckmann, 2008; Rykaczewski et al., 2008; Acevedo-Trejos et al., 2015). Consistently, the phyto-

63 plankton communities across the BUS feature a shift from the nearshore dominance of fast-grow-

64 ing species (e.g. diatoms) to more abundant small species (e.g. dinoflagellates) towards the open-

65 ocean (Barlow et al., 2005; Barlow et al., 2006; Wasmund et al., 2014). Recently, a seesaw behav-

66 ior between the abundance of the small- and the large-cell species across the BUS has been re-

67 ported (Lamont et al., 2019). This might be related to the fact that the coastal upwelling and the

68 WSCD upwelling are not necessarily in phase. In turn, they appear sometimes completely out of

69 phase (Jacox et al., 2018). Such a phase-relationship may drive systematic transitions from larger

70 species dominance to smaller species dominance or vice versa which can alter the structure of

71   the regional aquatic food web (Doney et al., 2012; Lamont et al., 2019). Hence, the relationship

72   between the rapid coastal upwelling and the slow WSCD upwelling is of vital importance for the

73   regional primary production.

74   Ekman coastal upwelling and that associated with the wind-stress-curl are not readily discernible

75   and often spatially overlapping (Lamont et al., 2019). More importantly, they are not the exclusive

76   drivers of the regional upwelling. Mesoscale and sub-mesoscale ageostrophic processes (e.g., ed-

77   dies, filaments, fronts, internal waves) play an important role in the time and space evolution of

78   the BUS through horizontal and vertical advection, shaping the nutrient distribution and enhanc-

79   ing mixing (Lass and Mohrholz 2008; Veitch et al., 2010; Bettencourt et al., 2012; Muller et al.,

80   2013; Veitch and Penven 2017; Lamont et al., 2019). For example, cyclonic sub-mesoscale eddies

81   intensify the upwelling and cause shoaling of the pycnocline/nutricline in the open-ocean waters.

82   The opposite is true for anti-cyclonic eddies (Lamont et al., 2019). Further, a strong horizontal

83   density contrast associated with coastal upwelling is formed at the base of the mixed layer depth

84   which largely influences mixing and diabatic processes (de Szoeke and Richman 1984). Also, flow-

85   topography interactions, coastal geometry, and cross-shore geostrophic transport may alter the

86   size and spatial pattern of the upwelling on different timescales (Mazzini and Bart, 2013). More-

87   over, the development and propagation of coastal Kelvin waves arising from alongshore wind-

88   stress variability can entirely shut down the coastal upwelling whereas it has little impact on the

89   offshore ocean dynamics (Fennel 1999; Fennel et al., 2012).

90   In this study, we explore the relationship between the temporal evolution of the coastal and the

91   WSCD upwelling. We also investigate the impacts of mesoscale and sub-mesoscale ocean dynam-

92   ics on these two types of upwelling and their relationship. To this end, we first examine the

93   upwelling estimated by using the analytical methodology based on Ekman theory applied to ob-

94   served surface wind data. We, additionally, analyze the output of a state-of-the-art forced ocean

95   circulation model with sufficiently high resolution to simulate mesoscale dynamics and partially

96   resolve sub-mesoscale instabilities. This allows us to examine how the interplay among different

97   upwelling drivers, which are excluded in the Ekman theory but captured by our numerical model

98   (eddies, filaments, fronts, internal waves), alters the regional upwelling and where the Ekman

99   theory can adequately represent the upwelling. Altogether, this approach is a trade-off between

100   the complexity of a full analytical solution (Fennel 1999) and missing contribution to upwelling

101   from processes not covered by the Ekman theory. With a particular focus on the phase difference,

102   we assess the relationship between the time evolution of rapid coastal upwelling and slow WSCD

103   upwelling in the Ekman theory together with the results of the high-resolution model.

104   Our paper is structured as follows. We first describe the observational data in section 2-1. Section

105   2-2 presents the model and our experimental set-up. The details of conceptual Ekman theory are

106   described in 2-3. The performance of the numerical model is evaluated by using different obser-

107   vational records in 3-1. Long-term means of the simulated and analytical upwelling are presented

108   in section 3-2. The spatial pattern of variability over the entire BUS and the linkage between

109   coastal and offshore (i.e., WSCD in the analytical theory and open-ocean in the model) upwelling

110   are discussed in section 3-3. The time series of coastal, analytical WSCD, and modeled open-ocean

111   upwelling for several cross-shore transects are displayed and discussed in section 3-4. We sum-

112   marize our results in section 4.

113

114

6

2- Methods and materials

2-1 Observational data

Among available surface wind products, we choose the observational wind at 10m height above the sea surface (U_{10}) from ASCAT products, in which C-Band scatterometer sensors were used to measure the ice-free ocean surface roughness (Ricciardulli and Wentz 2016). In fact, the surface roughness is a function of surface wind vectors. To retrieve the wind speed and direction from the ocean surface roughness, a numerical approach termed as Geophysical Model Function with a special focus on ASCAT records has been developed and used (Ricciardulli and Wentz 2016). The swath data are mapped on a 0.25°x0.25° regular grid and are daily composites from data of three days. Our analysis covers the 11-year period from 2008 to 2018. The climatological annual cycle of ASCAT wind vectors represents temporal and spatial patterns very consistent with other available observational wind products (Desbiolles et al., 2017). ASCAT mission is a running program with publicly accessible near-real-time data at the time of this study which facilitates the real-time estimate of wind-driven upwelling. Such a fast evaluation of the upwelling state meets the needs of researchers in different disciplines of ocean science who might need a real-time estimate of upwelling when they are on the cruise. We assumed a neutral boundary layer and calculated the wind-stress (τ) from the daily ASCAT wind and using the commonly-used bulk formula given by

$$\tau = \rho_a c_D \overrightarrow{U_{10}}.U_{10}. \tag{1}$$

ρ_a and c_D are surface air density and non-dimensional drag coefficient, respectively, and assumed to be constant at 1.23kgm^{-3} and 0.0013 (Gill 1982).

136   In addition, daily satellite-based Chlorophyll-a (Chl-a) concentration and Sea Surface Temperature

137   (SST) data sets with 4km spatial resolution were taken from MODIS-Aqua products (NASA

138   Goddard Space Flight Center 2018b). We also used the daily SST field from NOAA satellite OIv2

139   measurements (Reynolds et al., 2007). We mainly used the observed SSTs to validate the

140   performance of the model. To this end, we compute the SST-based upwelling index over the BUS.

141   This index is defined as the zonal SST contrast between coastal and open-ocean areas (Zhaoyun

142   et al., 2012; Benazzouz et al., 2014) as follow:

$$SST_{index} = SST_{coast} - \overline{SST_{open-ocean}} \tag{2}$$

144    $SST_{open-ocean}$ is computed as the average over 500-600km offshore.

145   High Chl-a values (>30 mg m^{-3}) are very likely biased in post-processing algorithms employing

146   atmospheric corrections (e.g., cloud coverage, fog, and aerosol dust) or due to nearshore turbid

147   water. As in similar studies (Thomas et al., 2012; Mohrholz et al., 2013), we considered the Chl-a

148   values near the coast, with cross-shore distance less than 9km, as well as suspiciously high values

149   (>30 mg m^{-3}) as noise and flagged them as missing values.

150   In order to validate the performance of the numerical model, AVISO daily satellite altimetry date

151   sets with 0.25° horizontal resolution for the 1993-2018 period (https://cds.climate.copernicus.eu)

152   along with daily tide gauge measurements from the University of Hawaii Sea Level Center

153   (https://uhslc.soest.hawaii.edu) are additionally used (Caldwell et al., 2015; Clementi et al.,

154   2019). Among different satellite altimetry products, absolute dynamic topography (ADT), defined

155   as the local deviation of sea surface height from the geoid, is chosen and analyzed. The deviation

156   of observed ADT and simulated sea surface height from their areal average over the model

157   domain are computed and termed as Dynamic Sea Level (DSL; Greatbatch, 1994; Bordbar et al.,

158   2015). The main reason for choosing the DSL comes back to the fact that we considered

159   Boussinesq approximation (i.e., conservation of volume rather than mass) in the model

160   simulation. Thus, sea-level displacement associated with changes in the density of the water

161   column is not properly captured by the model (Greatbatch, 1994). With respect to the tide gauge

162   records, time series of the research quality relative sea surface height from Simon's Town, Walvis

163   Bay, Port Sonara, Takoradi, Ascension Island, and Macae stations for the available time period

164   that matches the period of model simulation (i.e., 1992-2018) are analyzed.

165   We used the General Bathymetric Chart of the Oceans (GEBCO) data from https://www.gebco.net

166   in our numerical simulation (Fig. S1). The GEBCO seafloor bathymetry data was obtained from the

167   aggregation of a number of internationally and nationally measured or estimated seafloor

168   topography data by using General Mapping Tools (GMT) routines. These seafloor topographic

169   maps are mostly derived from direct measurements of single or multi-beam echo-sounders

170   during regular regional surveys. GEBCO has a spatial resolution of 15 arc seconds (GEBCO

171   Bathymetric Compilation Group, 2019). This data shows a shelf structure well comparable with

172   echo soundings from cruises. Several seamounts and deep canyons on the Namibian shelf (Fig.

173   S1) were identified as artifacts and were smoothed out using the etopo5-Data as reference.

174   **2-2 Ocean-Model Simulation**

175   We employed the Modular Ocean Circulation Model MOM-5, (Griffies, 2007), forced by

176   observational ocean-atmosphere momentum, heat and mass fluxes, and the river runoff. This

177   model is a B-grid hydrostatic model and is run using the Boussinesq approximation in our

178   integration. Prognostic variables are horizontal ocean velocity, sea-level elevation, conservative

179   temperature, and salinity. Vertical velocity is a diagnostic variable. Density and pressure in the

180   water column are calculated from the TEOS-10 equation of state in hydrostatic approximation.

181   For horizontal and vertical turbulent mixing, the Smagorinsky and the k-profile schemes were

182   employed (Large et al., 1994). The latter includes the diagnosis of a mixed and a mixing layer

183   depth. The vertical coordinates were z*-coordinate (Griffies, 2007), which reduces numerical

184   mixing from the undulating sea surface. The numerical integration was carried out with 1200

185   second baroclinic time step, the barotropic split is 100 seconds.

186   To account for the interaction between the tropical and subtropical Atlantic and impacts of the

187   South Atlantic subtropical gyre, Agulhas current, southeast Atlantic central water mass, the model

188   domain covers the Atlantic from 35°S to 12°N. Near the southwest African coast, which covers

189   the BUS region, the resolution in the east-west direction is approximately 5km and slowly

190   stretched to 15km westward. The latitudinal resolution is 5km in the BUS and extended to 8km

191   northward. The vertical resolution near the ocean surface is sufficiently high to capture internal

192   wave dynamics on the shelf. It starts from about 3m near the surface and reaches to about 10m

193   at 300m depth, but is further stretched below. Overall, the model consists of 118 vertical levels.

194   This experimental set-up is capable of adequately resolving the mesoscale and permits some sub-

195   mesoscale ocean dynamics (e.g. sub-mesoscale eddies and filaments), equatorial waves, coastal

196   trapped Kelvin waves, and associated mass and heat transports.

197   The time series of the main river discharges are taken from https://hybam.obs-mip.fr/. The ocean

198   bathymetry is taken from GEBCO and is mapped onto the model grid by bilinear interpolation.

199   The atmospheric momentum flux is estimated by using 6-hourly Cross-Calibrated Multi-Platform

200   (CCMP2) data with 0.25°x0.25° resolution (Atlas et al., 2011, Wentz et al. 2015). This data set was

201   obtained from a combination of several wind field products and covers a longer period compared

202   with ASCAT. Thus, forcing the model by CCMP2 data over a long period (i.e., 16 years) before the

203   onset of ASCAT records enables the model to reach a statistically equilibrium state in 2008.

204   CCMP2 wind products are not available as real-time data and are updated bi-annually. Across the

205   model domain, it shows very close values to ASCAT that is the base of our analytical consideration

206   over 2008-2018. Atmosphere-ocean heat and freshwater fluxes (i.e., evaporation and

207   precipitation) are estimated from ERA-interim reanalysis with 0.25°x0.25° horizontal resolution

208   using the bulk formulas of Beljaars et al. (1995). The prescribed quantities such as air pressure,

209   temperature, and humidity were converted into the ocean model horizontal grid using bilinear

210   interpolation. An exception is the wind field that was interpolated with the bicubic method to

211   reduce artifacts in the wind-stress-curl pattern induced by interpolation. It should be here

212   reminded that, unlike ASCAT data, CCMP2 includes wind field on lands. Such an interpolation

213   likely leads to a smooth transition from the land to the nearshore wind field. All fluxes are

214   calculated on the ocean model grid. The integration was carried out from 1992 to 2018. Here, we

215   mainly analyzed the model results between 2008 and 2018 and took the vertical velocity at the

216   base of mixed layer depth in the model output as the measure of upwelling intensity (McCreary

217   1981; Jacox et al., 2018).

218   The model employs open boundary conditions at the northern and southern boundaries. To

219   incorporate the impacts of physical processes outside the domain, the potential temperature and

220   salinity with 10-day time step and sea surface height with 12-hour time step were taken from the

221   ECCO (Estimating the Circulation and Climate of the Ocean) modelcube-92 (www.ecco-

222   group.org). Since Agulhas rings are obviously underestimated in the model (see Fig. 2) but known

223   to contribute significantly to the heat and mass transport over the very southern part of the BUS

11

224   (Veitch et al., 2010; Veitch and Penven 2017), we conjecture possible impacts on the upwelling

225   variability and take a very cautious interpretation of model results for this area.

226   We termed offshore upwelling in the model as open-ocean upwelling which is the equivalent of

227   WSCD upwelling in the analytical theory. Similar to previous model studies (Veitch et al., 2010;

228   Veitch and Penven 2017; Bonino et al., 2019), we use observed SST and the DSL to evaluate the

229   performance of the numerical model.

230   **2-3 Coastal and offshore upwelling**

231   According to the Ekman theory of wind-driven ocean circulation, ocean surface waters with

232   homogenous density structure subjected to a persistent surface wind stress undergo a steady

233   motion governed by a balance between the Coriolis force from their motion and wind-induced

234   vertical flux of horizontal momentum (Ekman 1905). The eastward (U_E) and northward (V_E)

235   vertically-integrated wind-driven volume transport per unit length is obtained as:

$$U_E = \frac{\tau^y}{\rho_w f} \qquad\qquad V_E = \frac{-\tau^x}{\rho_w f} \qquad\qquad (3)$$

237   ρ_w and f are seawater density and the Coriolis parameter, respectively. τ^x and τ^y are zonal and

238   meridional wind stress, respectively. f is negative on the southern hemisphere.

239   Southwest African coasts are overall meridionally oriented and features a dominant equatorward

240   surface atmospheric flow, which is persistent throughout the year and causes offshore transport

241   (Hart and Currie 1960; Shannon 1985; Small et al., 2015). Given the cross-shore divergence of the

242   transport near the coast, the displaced water is replaced by the convergence of alongshore

243   transport or by upwelled water into the Ekman layer (Mazinni et al., 2013; Muller et al., 2014;

244   Jacox et al., 2018). It is important to note that the Ekman balance is disturbed near the coast

245   (supplementary S-1). Due to the existence of the coast, the offshore transport and associated

246   divergence are compensated by vertically upwelled transport, when the alongshore current is

247   spatially uniform. This compensation of the divergence of the seaward flow by the vertical flow

248   occurs across an offshore distance of about the first baroclinic Rossby radius of deformation, R.

249   (McCreary 1981; Fennel, 1988, Fennel 1999; Mazinni et al., 2013; Jacox et al., 2018). Given the

250   fact that the Ekman balance is disturbed right at the coast, an additional surface transport

251   emerges which is in opposite direction to the Ekman transport and guaranties the coastal

252   boundary condition ($U(x = 0) = 0$; see Supplementary S-1). The small component from the

253   barotropic mode and variations of R from density changes due to upwelling (de Szoeke and

254   Richman 1984) is not considered here.

255   Independent of the presence of the coast, a spatially-heterogeneous wind field leads to a

256   divergence or convergence of the Ekman transport which additionally forces water in the upper

257   ocean to lift upward to the surface or pump downward to the deep ocean (Johnson 1976; Pickett

258   and Padaun 2003). In the f-plane approximation (i.e., f is assumed to be invariant with latitude),

259   this type of upwelling, referred to as Ekman pumping or WSCD upwelling (w_{curl}), reads:

$$w_{curl} = \frac{1}{\rho_w f}\left(\frac{\partial \tau^y}{\partial x} - \frac{\partial \tau^x}{\partial y}\right) \tag{4}$$

261   To compute the upwelling related to the coastal divergence (w_c), we first compute the Ekman

262   transport associated with surface wind field in each ocean grid point. To account for the effects

263   of coastal orientation on the cross-shore transport (Fig. S2), we compute the inner product

264   between the vector of coastal Ekman transport and the line orthogonal to the local coastline

265   which is termed the cross-shore Ekman transport ($U_{cross-shore}$; Pickett and Padaun 2003). One

266   should keep in mind that near the coast (x=0) the Ekman balance is disturbed (See Supplementary

13

267   S-1). In theory, if the meridional component of wind is considered as alongshore wind, $\frac{\tau^y_{x=0}}{\rho f}$ gives

268   the integrated coastal divergence of Ekman transport.

269   We utilized the observational-based R with 1°x1° resolution computed by Chelton et al. (1997). It

270   is particularly large over the northern sector of the BUS where the stratification is strong and f

271   (i.e., the Coriolis force) is relatively small (Fig. S3). We regrid this data with respect to ASCAT data

272   using the bilinear interpolation. If the Rossby radius of deformation near the coast was missing,

273   the value from the nearest grid point with the same latitude was used. The grid sizes are 0.25°

274   and smaller than R.

275   To compute the coastal upwelling from ASCAT data, we assume that, first, the total offshore

276   transport is compensated in a coastal distance equal to R and, second, the vertical velocity

277   decreases exponentially with cross-shore distance (Fennel 1999; Jacox et al., 2018). Given the

278   course resolution of ASCAT data, we assume the vertical water velocity in the coastal distance of

279   R decreases to 10% of the velocity near the coast. Thus, the velocity in the coastal distance smaller

280   than R is obtained using following formula (Supplementarry Info. Eq.22):

281
$$w_c = \frac{2.07 \times U_{cross-shore}}{R_1} e^{2.3026 \frac{x}{R_1}} \tag{5}$$

282   In which x and $U_{cross\text{-}shore}$ denotes the coastal distance and cross-shore Ekman transport,

283   respectively. Note that x is considered to be negative in east to west direction. At offshore

284   distances larger than R, the vertical velocity associated with coastal Ekman transport becomes

285   zero. This estimate is in a good agreement with theory of Benguela upwelling developed by Fennel

286   et al. (1999) (see Supplementary S1).

287   To compute the WSCD upwelling, we first calculate the wind-stress-curl. If a grid point on land

288   was involved, it was set to missing data. Thus, we excluded the nearest grid points to the coast

289   and computed the Ekman pumping elsewhere over the ocean.

290   The values of w_{curl} and w_c, were merged to a single date set and termed as "analytical theory".

291   Thus, within the coastal distance between 0.25° and R, the WSCD and coastal upwelling are

292   overlapping in the analytical approach. In theory, integrated coastal upwelling (W; Table S1) is

293   included both WSCD upwelling and the integrated coastal divergence of Ekman transport.

294   However, the contribution of WSCD upwelling in the nearest grid cell to the coast is neglected

295   here. The volume of upwelled water in each grid cell is estimated as the product of upwelling

296   velocity and grid-cell area. A summary of different upwelling related variables is given in table S1.

297   **3- Results and discussion**

298   In this section, we first compare the numerical model results with observational records to

299   validate model outputs. Thereafter, we assess the narrow band rapid coastal upwelling and slow

300   offshore upwelling along the southwestern coast of Africa (Fig. 1) with special interest in their

301   temporal relationship. In this context, we examine the spatial structure of the mean-state and

302   variability of the upwelling together with its temporal evolution in the model experiment and the

303   analytical theory.

304   **3-1 Model validation**

305   We first compare the mean-state and variability of the modeled and the observed DSL for the

306   1993-2018 period (Fig. 2). It stands for the large-scale circulation in the central water masses. The

307   variability is estimated from the Standard Deviation (Std) of 5-day mean values. In general, the

15

308   spatial pattern of the mean-state ocean topography, shown by the DSL, is well represented by the

309   model (Fig. 2). Important aspects of the large-scale ocean circulation such as zonal asymmetry

310   across tropical Atlantic, which is associated with equatorial currents and equatorial ocean

311   dynamics, the zonal contrast across the South Atlantic, which represents the strength and the

312   structure of the South Atlantic subtropical gyre, and relatively low sea level across the southwest

313   African coast are well reproduced by the model. The amplitude of the zonal contrast across the

314   southern sector is slightly underestimated by the model which means the subtropical gyre might

315   be weaker in the model. In addition, the eastward intrusion of the high DSL over the southern

316   sector is smaller in the model. The main difference is the high ocean topography over the

317   southwest Atlantic which is weaker and located further north in the model. With respect to the

318   spatial pattern of the variability, the model result compares fairly well with the satellite-derived

319   data. Large DSL variability over the western and eastern tropical Atlantic is well captured by the

320   model. The spatial pattern of modeled and observed variability over the southern sector shares

321   many similarities. However, the level of variability in this part is smaller in the model. The

322   variability of sea level elevation near the southern boundary of the model domain with Agulhas

323   current and associated rings is not well represented. Due to the numerical properties of the open

324   boundary conditions, water from the Indian Ocean enters the model domain too far west and

325   stays mostly away from the African coast. Relative to the observation, the simulated cold

326   upwelled water tends to extend farther seaward off the Cape Columbine cell (Fig. S4). This may

327   have some connections to the reduced Agulhas rings in the model. This limitation makes the

328   model simulation less reliable for the southernmost part of the BUS. For the rest of the domain,

329   the general pattern of SST mean-state and variability in the model and observation compare fairly

16

330   well (Fig. S4). Remarkable, the large meridional SST gradient over the ABFZ is captured well by the

331   model.

332   We also examine the time evolution of simulated DSL (Fig. S5,6). To this end, we first compare

333   the modeled DSL with several locally measured tide gauge records (Fig. S5). We also compare the

334   time series of 5-day mean modeled and observed DSL across several regions (Fig. S6). Overall, the

335   model simulation and tide gauge measurements are significantly correlated in all selected

336   stations. The correlation between the model and tide gauge records in Walvis Bay and Simon's

337   Port located within the BUS is about 0.59 and 0.47, respectively (Fig. S5). The areal average of

338   simulated and observed DSL over the western equatorial Atlantic, Atlantic Niño region, northern

339   and southern BUS are evolved very closely (Fig. S6). Overall, the model simulation can explain a

340   considerable part of the observed sea-level variability.

341   We additionally compare the spatial pattern of the mean-state and variability of the SST-based

342   upwelling index (see Methods) in the model and observation (Fig. S7). The modeled index is based

343   on water temperature at 1.5 depth, which is the shallowest vertical level of the model, whereas

344   it is based on SST in the observational estimates. In spite the fact that the observed SST is more

345   affected by local atmospheric forcing (i.e., radiation and evaporative cooling) the spatial pattern

346   of the observed and modeled mean and variability compare relatively well (Fig. S7). Remarkable

347   in this respect is the difference between the results of Aqua-Modis and Reynols SST which

348   suggests a large observational uncertainty. The time series of modeled and observed SST-based

349   index over the northern and southern BUS zones evolved very closely and represent significant

350   correlations (Fig. S7).

351

17

3-2 The upwelling mean-state

Figure 3 compares the spatial pattern of the annual mean (2008-2018) vertical water velocity, as a measure for the strength of upwelling, obtained from the numerical model and the analytical model. The long-time mean of remotely measured Chl-a concentration and surface wind fields are overlaid. In general, the simulated and analytical vertical velocities are broadly consistent in which coastal upwelling is generally intense over the entire domain and characterized by several distinct localized upwelling cells centered close to Kunene, Cape Frio, Walvis Bay, Lüderitz, and Cape Columbine. Kunene and Lüderitz coastal cells show more intense upwelling compared with other cells. This is in good agreement with previous studies (Lutjeharms and Meeuwis, 1987; Nicholson, 2010; Small et al., 2015; Jury 2017) and most likely due to the orography and the large localized land-sea temperature contrast, which can intensify the wind-stress locally. Despite the fact that the analytical consideration neglects several processes like propagation of coastally trapped Kelvin waves, topographic and coastal geometry impacts, cross-shore geostrophic flow, coastal upwelling in the model and analytical theory have very similar structures. With regard to the Kunene cell, the local subduction of Angola Current over the Angola-Benguela front can significantly reduce the upwelling locally which is not considered in the analytical theory. Overall, this result illustrates the dominant role of the coastal Ekman dynamics along the southwestern coast of Africa which can overshadow the impacts of other contributors on sufficiently long-term average. An exception is the Kunene upwelling cell, where the analytical approach gives much stronger coastal upwelling than the numerical model. This is partly due to poleward-directed Kelvin waves that tend to reduce coastal upwelling (Fennel, 1988, 1999). These Kelvin waves

373   arising from the strong meridional gradients in the meridional wind field that are neglected in our

374   analytical analysis.

375   An equatorward broadening of the open-ocean upwelling is an integral feature of the BUS (Fennel

376   et al., 2012) that is well reproduced by the model and analytical theory. Analogously, the

377   phytoplankton-rich belt (i.e., Chl-a concentration > 0.5 mg m^{-3}) along the coast widens up

378   equatorward. This provides a coherent signature with the structure of the wind-driven upwelling.

379   It also features two relatively wide bands centered near Orange River and slightly north of Walvis

380   Bay where the shelf widens (Fig. S1). It is worth noting that phytoplankton biomass is also

381   influenced by solar radiation, turbulent mixing, and nutrient flux (Lamont et al. 2019). Thus, such

382   a consistent spatial pattern underlines the profound impacts of physical upwelling which provides

383   the feeding opportunity for plankton communities. However, the offshore extension of the

384   upwelling region in the analytical theory and the numerical model are slightly different. The

385   offshore upwelling center between Lüderitz and Walvis Bay is slightly wider and stronger in the

386   numerical model with reference to the analytical theory. This difference might be attributed to

387   mesoscale and sub-mesoscale ocean processes across the region impacting the vertical water

388   transport (Bettencourt et al. 2012). However, this result reflects the prevailing impact of Ekman

389   dynamics compared with other drivers of the upwelling over the long-term average across the

390   southwest African coast.

391   Over the coastal distance of R, the coastal and the WSCD upwelling overlap. It is important once

392   again to bear in mind that the wind-stress-curl in the nearest grid cell to the coast was set to the

393   missing value in our analytical theory. Hence, the contribution of the coastal and WSCD upwelling

394   can be quantified over limited area north of Walvis Bay (Fig S8). North of Walvis Bay and near the

395   northernmost sector of the BUS, a significant proportion of the nearshore upwelling is associated

396   with the WSCD upwelling (Fig. S8). Given the horizontal resolution of ASCAT data compared with

397   the local R, a reliable estimate of this contribution with adequately high spatial resolution remains

398   a challenge.

399   Fig. 4 displays the annual average of vertical water velocity from the model and the analytical

400   theory, the observed Chl-a concentration, meridional surface wind velocity together with ocean

401   depth in seven cross-shore transects. Sign and magnitude of the wind-stress-curl across the BUS

402   are determined to a great extent by the zonal variation of the meridional wind velocity (Fennel et

403   al. 2012). The coastal drop-off in the meridional wind velocity is the major contribution to the

404   wind-stress-curl. It occurs over narrower bands in the southern BUS (Hondeklip Bay, Cape

405   Columbine) but extends much further offshore in the northern BUS (Cape Frio, Walvis Bay). A

406   particular exception to that is found off the Kunene mouth, where the wind starts to decline near

407   the coast (Fig. 4a). Despite the simplicity of the analytical approach, its outcome shares many

408   similarities with the numerical model results. This reflects the dominant role of Ekman dynamics

409   across the entire BUS on the long-time average. In general, the analytical theory renders larger

410   values near the coast relative to the model output. This difference is more pronounced in the

411   Kunene, Cape Frio, and Orange River cells. This overvaluation is potentially due to the spatially

412   coarse resolution of the ASCAT observed wind field (0.25°x25°) which prohibits an adequately

413   fine-resolution estimate of coastal upwelling. As pointed out by Lamont et al. (2019), a steep

414   inshore-offshore gradient in Chl-a concentration, associated with the seaward reduction of the

415   vertical water velocity, is revealed in all transects. The nearshore Chl-a concentration in Walvis

20

416   Bay, Orange River, and Cape Columbine, where the continental shelf is relatively broad, appears

417   to be large compared with other transects.

3-3 The upwelling variability

419   To get an overview of the upwelling variability and to further check the consistency between the

420   model and our analytical approach, we next examine the Std of the simulated and analytical

421   monthly mean vertical water velocities as a measure for the variability (Fig. 5). Unlike the spatial

422   pattern of the long-term mean (Fig. 3), the spatial maps of variability computed from the model

423   and analytical theory show remarkable differences. The model offshore variability across the

424   entire domain is nearly one order of magnitude larger than that derived from the analytical

425   approach (Fig. 5a,b). The presence of sub-mesoscale filaments and eddies across the region could

426   be very likely behind this difference (Bettencourt et al. 2012). In fact, sub-mesoscale dynamics is

427   known to exert profound influences on the near-surface vertical velocity, and associated upward

428   nutrition flux into the euphotic layer, which is not taken into account in the analytical estimate.

429   Offshore waters near Walvis Bay and Lüderitz and across the southwestern BUS appear to have

430   high variability in the model. Giving the uncertainty associated with boundary values near the

431   southern sector, it is reasonable to place a caveat on the interpretation of model outputs very

432   close to the southern part of the domain. Large variability in the proximity of the Lüderitz cell

433   might be connected to the year-round occurrence of strong filaments with a large vertical extent

434   and accompanied with the perennial alongshore wind (Hösen et al., 2016; Veitch and Penven

435   2017). Consistent with the model result, a large vertical displacement of thermocline associated

436   with seaward propagation of sub-mesoscale filaments, eddies, and Rossby waves near Walvis Bay

437   was previously reported by Mohrholz et al. (2008).

In the following section, we investigate the temporal evolution of the simulated and the analytical upwelling in more detail and examine to what extent Ekman dynamics can estimate the amount of upwelled waters across the southern and northern sub-systems. We begin with the linear correlation between simulated and analytical upwelling in each grid point (Fig. 6a). In general, the correlation peaks near the coast which is typically larger than 0.6 everywhere nearshore; implying that the simulated (w_m) and analytical coastal upwelling (w_c) evolved very closely. The large agreement between model and analytical theory near the coast further reflects the fundamental role of the coastal Ekman drift and associated upwelling near the coast. With respect to the open-ocean upwelling which is exclusively WSCD in the analytical approach (i.e., w_{curl}), except over the southern sector of the BUS near Cape Columbine, the correlation between the simulated and analytical upwelling is mostly weak and not statistically significant (Fig. 6a). Since the variability associated with the Agulhas rings seems to be underestimated in the model, it is difficult to make any definite statement about the relatively high correlation over the southern part of the domain. Near Lüderitz and Walvis Bay, where a large offshore variability is simulated (Fig. 5a), the correlation is not statistically significant. This result suggests that the upwelling associated with wind-stress-curl is largely disrupted by the local mesoscale and sub-mesoscale dynamics.

However, the time series of the simulated ($V_{m\text{-offshore}}$) and the analytical (V_{curl}) vertical volume transport offshore across the entire domain behave closely with the correlation of about 0.47 (Fig. 6b). Despite the interruptive effects of mesoscale and sub-mesoscale dynamics on small scales, its impacts over the entire domain seem to be small and the basin-wide vertical water transport estimated by Ekman theory is still consistent with model results. This close time evolution is also found in the upwelling across the southern and the northern sub-systems (Fig.

460   6c-d), which render statistically significant correlations of 0.71 and 0.45, respectively. The

461   relatively weak correlation in the northern sub-system can be partly explained by the large local

462   sub-mesoscale activities (Fig. 5a). Given the mesoscale corridors associated with Agulhas leakage

463   near the southern flank, one expects the disruptive role of sub-mesoscale dynamics over the

464   southern BUS to be larger relative to that in the north, but the results of the numerical model

465   reveal otherwise.

466   Further, the amount of upwelled water from the analytical consideration appears to be often

467   larger than simulated upwelling over the northern BUS. This is consistent with previous model

468   studies noting that the amount of upwelled water across the eastern boundary upwelling systems

469   is, in general, reduced when mesoscale and sub-mesoscale activities are represented in the model

470   (Capet et al. 2008). This effect can be attributed to the eddy-induced subductions in the upper-

471   oceanic fronts.

472   **3-4 Time evolution of the coastal and the open-ocean upwelling**

473   This section is devoted to the time evolution of the coastal upwelling and the open-ocean

474   upwelling. The latter is exclusively WSCD upwelling in the analytical approach. With a particular

475   interest in the phase difference, we aim to determine whether these components of upwelling

476   evolve coherently or alternating with each other. Here, we recall that local processes such as the

477   thermal coupling between ocean and atmosphere, feedbacks between the crosswind SST

478   gradient and the wind-stress-curl, orographic effects, and the coastal geometry play significant

479   roles in these relationships (Desbiolles et al., 2014). Figure 7-a displays the linear correlation

480   coefficient between coastal (i.e., w_c) and WSCD (i.e., w_{curl}) upwelling being at the same latitude in

481   the analytical theory.

482   The coastal and the WSCD upwelling are mostly anti-correlated north of Lüderitz. This feature is

483   more obvious and statistically significant near the Kunene cell. Theoretically, it indicates that a

484   weakening of the coastal upwelling is often concurrent with an intensification of the WSCD

485   upwelling and vice versa. From the south of Cape Frio to the north of Lüderitz, the area with the

486   statistically significant anti-correlation is limited to a relatively narrow band near the coast. Such

487   an inverse relationship gradually disappears nearly south of Lüderitz and the correlation becomes

488   positive and statistically significant from the north of Hondeklip Bay to the south of Cape

489   Columbine which suggests the coastal and the WSCD upwelling often evolve nearly in phase. Part

490   of this behavior is very likely connected to the seasonal cycle of the wind field. Concurrent with

491   seasonally strong wind-stress-curl from October to April over the entire domain, the alongshore

492   component of wind is stronger in the southern BUS but weaker in the far north (Fig. S9-S10). The

493   correlation between upwelling anomalies yields the same structure but with a smaller magnitude

494   (Fig. S11). In particular, the reduction in the size of correlation is more pronounced off Cape

495   Columbine and Hondeklip Bay cells where the seasonal variation of the wind is relatively strong

496   (Fig. S9). Overall, this result suggests that the annual cycle has a contrasting impact on the

497   relationship between coastal and WSCD upwelling in the northern and the southern sub-systems.

498   During different seasons, the spatial structure of the correlation and, thus, the phase difference

499   might be different. To this end, we computed the aforementioned correlation for the periods

500   corresponding to Nov-Mar and May-Sep (Fig. 7b-c). The general structure does not change much.

501   Note that the statistical degrees of freedom in Fig. 7b-c is different from Fig. 7a; meaning the

502   same level of correlation does not necessarily indicate the same level of statistical confidence.

503   From visual inspection, the magnitude of correlation coefficient near the Kunene cell appears to

504   be larger between May and September which is concurrent with the local intensification of the

505   alongshore winds and weakening of the wind-stress-curl (Fig. S9-10). Thus, the seesaw behavior

506   is likely to be stronger between May-September.

507   The spatial pattern of the correlation in the model is very noisy (Fig. S12). Apparently, the

508   correlation pattern is strongly disrupted by sub-mesoscale ocean dynamics. The inevitable

509   question that arises is whether the mesoscale and sub-mesoscale dynamics remarkably alter the

510   relationship between the amount of coastal (w_c) and WSCD upwelled water. In this way, we

511   discuss here the time series of coastal ($V_{m-coast}$) and open-ocean ($V_{m-offshore}$) volume of upwelled

512   water and their climatological annual cycle computed over seven sub-regions of the BUS (Fig. 8-

513   9). These regions are shown by rectangular boxes in Fig. 6a.

514   The seasonal cycle of coastal upwelling in Kunene is characterized by a biannual cycle. The coastal

515   upwelling peaks in June and October; whereas the open-ocean upwelling is identified by rather a

516   mirror-like pattern with its minimum in July and October (Fig. 8a). This behavior is consistent with

517   the annual cycle of the alongshore wind and the wind-stress-curl (Fig. S9,10). 57% of the coastal

518   upwelling variability can be explained by the annual cycle (see Table 1). This feature is less

519   pronounced for the open-ocean upwelling (14%; Table 1). This might be connected to the

520   dominant role of the Ekman transport in the coastal upwelling whereas any changes in the

521   strength and direction of coastal or offshore winds can significantly alter the size of WSCD

522   upwelling. Similar to the annual cycles (Fig. 8a), coastal and open-ocean upwelling anomalies off

523   Kunene frequently appear in opposite phases, with correlation of about -0.24 (Fig. 8b). In fact,

524   positive and negative peaks in the coastal and the open-ocean time series frequently alternate

525   with each other. The open-ocean upwelling events are mostly associated with opposite-sign

526   anomalies in the coastal upwelling. This is in accordance with the correlation pattern obtained

527   from the analytical consideration (Fig. 7; Fig. S11).

528   Off Cape Frio, the biannual cycle is less pronounced compared to the Kunene cell (Fig. 8c). Coastal

529   and open-ocean upwelling are often in opposite phases (Fig. 8c,d). Again, extreme events of the

530   open-ocean upwelling are mostly concurrent with opposite-sign peaks in the coastal upwelling

531   and vice versa (Fig. 8d). However, this opposite-phase relationship seems to be less pronounced

532   compared with the Kunene cell. Again, this is in agreement with the result of analytical theory

533   (Fig. 7a). Moreover, the correlation between coastal upwelled water in Cape Frio and Kunene is

534   nearly 0.8. This further highlights the notion that these two upwelling cells can be considered as

535   a single cell in terms of coastal upwelling (Lutjeharms and Meeuwis 1987; Jury 2017). However,

536   this correlation for the offshore upwelled water and the corresponding annual cycle is relatively

537   weak (0.27).

538   Fluctuations of the coastal and open-ocean upwelling are dominated by a discernible annual cycle

539   in Walvis Bay with the explained variability of about 72% and 36%, respectively (Fig. 8e; Table 1).

540   The coastal and open-ocean upwelling annual cycles are very similar. They peak in August and

541   July, respectively (Fig. 8e). Strong and weak upwelling anomalies appear frequently concurrent,

542   with the anomaly correlation coefficient of about 0.22 (Fig. 8f). This correlation is rather

543   ambiguous for the analytical theory. From the coast towards the ocean, the correlation changes

544   the sign (Fig. S11). In the vicinity of the coast, the coastal and the WSCD upwelling anomalies are

545   positively correlated whereas they are anti-correlated farther offshore. It should be recalled that

546   an intensive mesoscale and sub-mesoscale dynamics is simulated off Walvis Bay which can largely

26

547   modulate the offshore upwelling and influence the relationship between the coastal and the

548   WSCD upwelling.

549   Significant parts of coastal and open-ocean upwelling variability in the Lüderitz cell can be

550   explained by the seasonal variation (Table 1). The seasonal cycles are in phase between December

551   and July and nearly in opposite phase between August and October (Fig. 8g). Similar to other

552   stations, the annual cycle is more pronounced in the coastal upwelling (Table 1). The correlation

553   between the upwelling anomalies is not statistically significant and the phase difference between

554   them seems not to follow a rigid pattern (Fig. 8h).

555   In summary, the correlation across the coastal upwelling in different stations in the northern BUS

556   (i.e., Kunene, Cape Frio, Walvis Bay) is large and statistically significant, whereas the correlation

557   derived from the open-ocean upwelling across different upwelling cells is generally weak and

558   often not statistically significant.

559   Time series of the coastal and the open-ocean upwelling across Orange River, Hondeklip Bay, and

560   Cape Columbine, located in the southern BUS, are shown in Fig. 9. The contribution of the annual

561   cycle in total variability of the coastal upwelled water is large but slightly smaller than in the

562   northern BUS (Table 1). The amount of the open-ocean upwelled water off Orange River is

563   associated with a strong seasonal cycle explaining about 44% of the total variability (Fig. 9a; Table

564   1). The open-ocean upwelling peaks between December and March when the coastal upwelling

565   appears to be very close to its annual average (Fig. 9a). Between August and October, the coastal

566   upwelling peaks whereas its counterpart experiences its annual minimum (Fig. 9a). Given the

567   large contribution of the seasonal cycle in the total variability of coastal and open-ocean

568   upwelling off Orange River (Table 1) the phase difference between them seems to be strongly

569   seasonally dependent. The anomaly correlation between the coastal and the open-ocean

570   upwelling off Orange River is about 0.23.

571   Off Hondeklip Bay, the contribution of the seasonal cycle in the total variability of the coastal and

572   the open-ocean upwelling is about 44% and 16%, respectively. From November to July, the coastal

573   and the open-ocean upwelling evolve rather coherently whereas they are frequently in opposite

574   phases between August and October (Fig. 9c). Again, the relationship between coastal and open-

575   ocean off Hondeklip Bay seems to be seasonally dependent but less pronounced compared with

576   that in the Orange River cell. The correlation between the time series of upwelling anomalies is

577   very small and not statistically significant (Fig. 9d).

578   With regard to Cape Columbine, which is the southernmost selected station in this study, 66% of

579   the open-ocean upwelling variability can be explained by the seasonal cycle alone (Table 1). The

580   open-ocean and the coastal upwelling peaks at different times of the year (Fig. 9e). The coastal

581   (open-ocean) upwelling peaks in October (March-April) and reaches its minimum in May (August-

582   September). Overall, the correlation between the open-ocean and the coastal upwelling

583   anomalies is about 0.20 and statistically significant which is consistent with the result of the

584   analytical consideration. Given the underestimated Agulhas rings in the model, the found

585   relationship between the coastal and the open-ocean upwelling in the vicinity of the Agulhas Bank

586   (i.e., Cape Columbine upwelling cell) is likely to be spurious.

587   **4- Summary and conclusions**

588   Using results of a state-of-the-art eddy-resolving ocean circulation model along with a linearized

589   analytical approach for a simplified parameterization of wind-driven upwelling, the time and

590   space variations of the water vertical velocity along the southwest African coast as far as Benguela

28

591   Upwelling System (BUS) were investigated for the 2008-2018 period. Satellite-derived Chl-a

592   concentration was additionally analyzed.

593   In terms of the mean-state, the model and analytical approach agreed fairly well in which the

594   intense upwelling associated with the coastal divergence of Ekman transport appeared to be the

595   dominant factor across the entire BUS. The northward expansion of the offshore upwelling,

596   supported by the theory of the BUS, was captured by the model and the analytical consideration.

597   Remarkable in this respect is the spatial pattern of Chl-a concentration which compares relatively

598   well with the spatial pattern of the upwelling.

599   In agreement with previous studies, the model-based results revealed vigorous mesoscale and

600   sub-mesoscale activities (e.g., filaments and eddies) in the open-ocean domains with more

601   pronounced signatures over the northern subsystem off Lüderitz and Walvis Bay (Bettencourt et

602   al. 2012). We found these activities exert profound impacts on the wind-stress-curl-driven

603   (WSCD) upwelling and substantially enhance its variability. Despite the interruptive impacts of

604   mesoscale and sub-mesoscale activities on the WSCD upwelling in the model, the consistency

605   between model and analytical theory in terms of the total volume of upwelled water was

606   retained. This result indicates that using near-real-time wind data in the analytical approach can

607   provide a fast and reliable evaluation of the upwelling state for marine researchers who might

608   need a real-time estimate of upwelling.

609   Also, our study shows that in terms of coastal upwelling, Kunene and Cape Frio cells can be

610   considered as a single cell. However, WSCD upwelling across these cells showed some differences.

611   We found an overall inverse relationship between the time evolution of the coastal and the WSCD

612   upwelling in Kunene and Cape Frio. It indicates that the WSCD and the coastal upwelling

613   frequently alternate each other which implies that the weakening of one is very likely associated

614   with the strengthening of another. Hence, the abundance of nearshore large-cell phytoplankton

615   and open-ocean small-cell phytoplanktons are expected to have a seesaw behavior that can

616   largely regulate the marine food web.

617   In contrast, the coastal and open-ocean upwelling in Walvis Bay are identified with clear annual

618   cycles and are frequently in phase. At the same time, the phase difference between the coastal

619   and the open-ocean upwelling off Lüderitz appear to be strongly seasonally dependent. Like

620   Lüderitz, the relationship between these two types of upwelling across the southern BUS varied

621   seasonally. As opposed to the northern part of the domain, the coastal and open-ocean upwelling

622   of the southernmost sector of the BUS (i.e. Cape Columbine) closely followed each other. Overall,

623   our results suggest that the time evolution of upwelling across the BUS is far more complicated

624   than currently thought.

625   Owing to the horizontal resolution of ASCAT gridded records which is 0.25°, an accurate estimate

626   of coastal wind drop-off, which is typically within a few 10km offshore distance, still remains an

627   issue of concern. To develop a more comprehensive understanding of this term and the

628   connections between the coastal and WSCD upwelling, using a high-resolution regional

629   atmospheric model simulation would be very beneficial. Our results further support the notion

630   that local wind forcing, among other local and remote upwelling drivers (i.e., coastally trapped

631   waves, thermocline variations, mixing), largely regulates the regional upwelling across the BUS.

632   Thus, migration of the South Atlantic high-pressure system or changes in the sea level pressure

633   pattern over the African continent would lead to change in the magnitude, timing, and structure

634   of upwelling across the BUS. With current satellite-based Chl-a data, a reliable estimate of climatic

635   changes driven fluctuations in the plankton size structure, which is equally important as the total

636   biomass for the marine ecologists and biologists, appears a big challenge. Hence, it seems

637   essential to work towards a comprehensive monitoring system based on the size structure of

638   planktons. Incontrovertible evidence for human-induced climate changes has become more

639   frequent (IPCC 2014; Bordbar et al., 2015, 2019) which might have short- and far-reaching

640   implications for the pelagic marine ecosystems across the BUS.

649   **Conflicts of Interest**

650   The authors declare no conflict of interest.

651   **Data availability**

652   Data shown in this manuscript are available by email from corresponding author (hadi.bordbar@io-

653   warnemuende.de).

654

655

References

657 Acevedo-Trejos, E., G. Brandt, J. Bruggeman, and A. Merico, 2015: Mechanisms shaping size

658 structure and functional diversity of phytoplankton communities in the ocean. *Sci. Rep.* **5**, 8918,

659 doi.org/10.1038/srep08918.

660 Atlas, R., R. N. Hoffman, J. Ardizzone, S. M. Leidner, J. C. Jusem, D. K. Smith, and D. Gombos,

661 2011: A cross-calibrated, multiplatform ocean surface wind velocity product for meteorological

662 and oceanographic applications. *Bull. Amer. Meteor. Soc.*, **92**, 157-174. doi:

663 10.1175/2010BAMS2946.1

664 Bachelery, M. L., S. Illig, and I. Dadou, 2016: Interannual variability in the South-East Atlantic

665 Ocean, focusing on the Benguela Upwelling System: Remote versus local forcing, *J. Geophys.*

666 *Res. Oceans,* **121**, 284–310, doi:10.1002/2015JC011168.

667 Bakun, A., and C. S. Nelson, 1991: The seasonal cycle of wind stress curl in the sub-tropical

668 eastern boundary current regions. *J. Phys. Oceanogr.* **21**, 1815–1834.

669 Barlow, R., H. Sessions, M. Balarin, S. Weeks, C. Whittle, and L. Hutchings, 2005: Seasonal

670 variation in phytoplankton in the southern Benguela: pigment indices and ocean colour. *S. Afr. J.*

671 *Mar. Sci.* **27**, 275–288, doi.org/10.2989/18142320509504086.

672 Barlow, R., D. Louw, M. Balarin, and J. Alheit, 2006: Pigment signatures of phytoplankton

673 composition in the northern Benguela ecosystem during spring. *African Journal of Marine*

674 *Science.* **28**(3&4), doi.10.2989/18142320609504200.

675 Barros, V.R., et al., 2014: *IPCC Climate Change, Impacts, Adaptation, and Vulnerability. Part B:*

676 *Regional Aspects. Contribution of Working Group II to the Fifth Assessment Report of the*

Accepted for publication in *Journal of Physical Oceanography*. DOI 10.1175/JPO-D-20-0297.1.

32

Intergovernmental Panel on Climate Change. Cambridge University Press, Cambridge, United Kingdom and New York, NY, USA, pp. 688.

Beljaars, A. C. M., 1995: The parametrization of surface fluxes in large-scale models under free convection. *Q. J. R. Meteorol. Soc.* **121**, 255–270, doi.10.1256/smsqj.52202.

Benazzouz A, S. Mordanea, A. Orbib, M. Chagdalia, K. Hilmib, A. Atillahc, J. L. Pelegríd, D. Hervée, 2014: An improved coastal upwelling index from sea surface temperature using satellite-based approach – the case of the Canary Current upwelling system. *Cont. Shelf. Res.* **81**, 38–54. doi: 10.1016/j.csr.2014.03.012

Bettencourt, J. H., C. López, and E. Hernández-García, 2012: Oceanic three-dimensional Lagrangian coherent structures: A study of a mesoscale eddy in the Benguela upwelling region. *Ocean Modelling*, **51**, 73–83.

Bonino, G., E. Di Lorenzo, S. Masina, D. Iovino, 2019: Interannual to decadal variability within and across the major Eastern Boundary Upwelling Systems. Sci Rep 9, 19949, doi.org/10.1038/s41598-019-56514-8.

Bordbar, M. H., T. Martin, M. Latif, and W. Park, 2015: Effects of long-term variability on projections of twenty-first-century dynamic sea level, *Nat. Clim. Change*, **5**, 343–347.

Bordbar, M. H., M. H. England, A. Sen Gupta, A. Santoso, A. S. Taschetto, T. Martin, W. Park, and M. Latif, 2019: Uncertainty in near-term global surface warming linked to tropical Pacific climate variability. *Nat. Commun.*, **10**, 1990, doi.org/10.1038/s41467-019-09761-2.

696   Caldwell, P. C., M. A. Merrifield, P. R. Thompson, 2015: Sea level measured by tide gauges from global

697   oceans — the Joint Archive for Sea Level holdings (NCEI Accession 0019568), Version 5.5, *NOAA National*

698   *Centers for Environmental Information*, Dataset, doi:10.7289/V5V40S7W.

699   Capet, X., F. Colas, J. C. McWilliams, P. Penven, and P. Marchesiello, 2008: Eddies in eastern

700   boundary subtropical upwelling systems. *Ocean Model.* Eddying Regime Geophys. Monogr. Ser

701   **177**, 131–147.

702   Clementi, E., et al., 2019: Mediterranean Sea Analysis and Forecast (CMEMS MED-Currents, EAS5 system)

703   [Data set]. Copernicus Marine Environment Monitoring Service (CMEMS). DOI:

704   https://doi.org/10.25423/CMCC/MEDSEA_ANALYSIS_FORECAST_PHY_006_013_EAS5.

705   Chelton, D. B, R. A. DeSzoeke, and M. G. Schlax, 1998: Geographical variability of the first

706   baroclinic Rossby radius of deformation. *J. Phy. Oceanog.* **28**, 443-460.

707   Desbiolles, F., B. Blanke, A. Bentamy, and N. Grima, 2014: Origin of finescale wind stress curl

708   structures in the Benguela and Canary upwelling systems, *J. Geophys. Res. Oceans*, **119**, 7931–

709   7948, doi:10.1002/2014JC010015.

710   Desbiolles F. et al., 2017: Two decades [1992–2012] of surface wind analyses based on satellite

711   scatterometer observations. *J. of Marine Systems*, **168**, 38-56,

712   doi.org/10.1016/j.jmarsys.2017.01.003.

713   de Szoeke, R. A., and R. Richman, 1984: On wind-driven mixed layers with strong horizontal

714   gradients—a theory with application to coastal upwelling. *J. Phys. Oceanogr.,* **14**, 364–377.

715   Doney, S. C. et al. 2012: Climate change impacts on marine ecosystems. *Annu. Rev. Mar. Sci.* **4**,

716   11–37. Doi: 10.1146/annurev-marine-041911-111611.

717   Duncombe Rae, C. M., 2005: A demonstration of the hydrographic partition of the Benguela

718   upwelling ecosystem at 26°40'S. *African Journal of Marine Science,* **27**(3), 617-628.

719   Ekman V. W., 1905: On the influence of the Earth's rotation on ocean currents. *Arkiv for*

720   *Matematik, Astronomi, och Fysik*., **2** (11).

721   Fennel, W., 1988. Analytical Theory of the Steady State Coastal Ocean and Equatorial Ocean,

722   Journal of Physical Oceanography, 18(6), 834-850. Retrieved Mar 7, 2021, from

723   https://journals.ametsoc.org/view/journals/phoc/18/6/1520-

724   0485_1988_018_0834_atotss_2_0_co_2.xml

725   Fennel, W., 1999: Theory of the Benguela Upwelling System. *J. Phy. Oceanog.* **29**, 177-190.

726   Fennel, W. and H. U. Lass, 2007: On the impact of wind curls on coastal currents. *J. Mar. Syst.*

727   **68**, 128–142.

728   Fennel, W., T. Junker, M. Schmidt, and V. Mohrholz, 2012: Response of the Benguela upwelling

729   systems to spatial variations in the wind stress. *Continental Shelf Research*. **45**, 65–77,

730   doi.org/10.1016/j.csr.2012.06.004.

731   GEBCO Bathymetric Compilation Group, 2019: The GEBCO_2019 Grid - a continuous terrain

732   model of the global oceans and land. British Oceanographic Data Centre, National

733   Oceanography Centre, NERC, UK. doi:10/c33m.

734   Gill, A. E., 1982: *Atmosphere-Ocean Dynamics*. Academic, San Diego, Calif.

735   Greatbatch, R, 1994: A note on the representation of steric sea level in models that conserve

736   volume rather than mass. J. *Geophys. Res. Oceans,* **99,** 12767-12771.

737   Griffies, S. M., 2012: ELEMENTS OF MOM. GFDL OCEAN GROUP. Technical Report No. 7.

738   NOAA/Geophysical Fluid Dynamics Laboratory. Available on-line at https://mom-

739   ocean.github.io.

740   Hösen, E., J. Möller, K. Jochumsen, and D. Quadfasel, 2016: Scales and properties of cold

741   filaments in the Benguela upwelling system off Lüderitz, J. *Geophys. Res. Oceans*, **121**, 1896–

742   1913, doi:10.1002/2015JC011411.

743   Hutchings, L., et al., 2009: The Benguela Current: an ecosystem of four components. *Progress in*

744   *Oceanography*, **83**(1-4), 15-32.

745   Jacox, M. G., C. A. Edwards, E. L. Hazen, and S. J. Bograd, 2018: Coastal upwelling revisited:

746   Ekman, Bakun, and improved upwelling indices for the U.S. West Coast. *Journal of Geophysical*

747   *Research: Oceans*, **123**, 7332–7350, doi.org/10.1029/2018JC014187.

748   Johnson, J.A., 1976: Modifications of coastal currents and upwelling by off-shore variations in

749   wind stress. *Tellus*, **28** (3), 254–260, doi.org/10.1111/j.2153-3490.1976. tb00673.x.

750   Junker, T., M. Schmidt, and V. Mohrholz, 2015: The relation of wind stress curl and meridional

751   transport in the Benguela upwelling system. *Journal of Marine Systems*, **143**, 1-6,

752   doi.org/10.1016/j.jmarsys.2014.10.006.

753   Junker, T., V. Mohrholz, L. Siegfried, and A. van der Plas, 2017: Seasonal to interannual

754   variability of water mass characteristics and currents on the Namibian shelf. *J. Mar. Syst.*, **165**,

755   36-46, doi. 10.1016/j.jmarsys.2016.09.003.

756   Jury, M. R., 2017: Coastal upwelling at Cape Frio: Its structure and weakening. *Continental Shelf*

757   *Research*, **132**, 19-28, doi.org/10.1016/j.csr.2016.11.009.

758   Koseki, S., H. Giordani, and K. Goubanova, 2019: Frontogenesis of the Angola–Benguela Frontal

759   Zone. *Ocean. Sci.*, **15**, 83–96.

760   Lamont, T., R. G. Barlow, and R. J. Brewin, 2019: Long-Term Trends in Phytoplankton Chlorophyll

761   a and Size Structure in the Benguela Upwelling System. *Journal of Geophysical Research: Ocean*,

762   **124**, 1170-1195, doi.org/10.1029/2018JC014334.

763   Large, W.G., J. C. McWilliams, and S. C. Doney, 1994: Oceanic vertical mixing: a review and a

764   model with a nonlocal boundary layer parameterization. *Review of Geophysics*, **32**, 363–403.

765   Lass, H. U., and V. Mohrholz, 2008: On the interaction between the subtropical gyre and the

766   subtropical cell on the shelf of the SE Atlantic. *J. Mar. Syst.*, **74**, 1–43,

767   doi.org/10.1016/j.jmarsys.2007.09.008.

768   Louw, D., K. Anja, V. Mohrholz, N. Wasmund, T. Junker, and A. Eggert, 2016: Seasonal and inter-

769   annual phytoplankton dynamics and forcing mechanisms in the northern Benguela upwelling

770   system. *J. Mar. Sys.*, **157**, 124 –134, doi/10.1016/j.jmarsys.2016.01.009.

771   Lutjeharms, J. R. E. and J. M. Meeuwis, 1987: The extent and variability of South-East Atlantic

772   upwelling. *S. Afr. J. Mar. Sci.*, **5**, 51-62, doi:10.2989/025776187784522621.

773   Lübbecke, J. F., C. W. Böning, N. S. Keenlyside, and S. P. Xie, 2010: On the connection between

774   Benguela and equatorial Atlantic Niños and the role of the South Atlantic Anticyclone. *J. of*

775   *Geophysical Research*, **115**, C09015, doi:10.1029/2009JC005964.

776   Lübbecke, J. F., P. Brandt, and M. Dengler, 2019: Causes and evolution of the southeastern

777   tropical Atlantic warm event in early 2016. *Clim. Dyn.,* **53**, 261–274, doi.org/10.1007/s00382-

778   018-4582-8.

779   Mazzini, P. L. F., and J. A. Barth, 2013: A comparison of mechanisms generating vertical

780   transport in the Brazilian coastal upwelling regions. *J. Geophys. Res. Oceans*, **118**, 5977–5993,

781   doi:10.1002/2013JC008924.

782   McCreary, J. P., 1981: A linear stratified ocean model of the coastal undercurrent. *Philos. Trans.*

783   *Roy. Soc. London*, Series A, **302**, 385–413.

784   Mohrholz, V., C. H. Bartholomae, A. K. van der Plas, H. U. Lass, 2008: The seasonal variability of

785   the northern Benguela undercurrent and its relation to the oxygen budget on the shelf.

786   *Continental Shelf Research*, **28**, 424–441, doi.org/10.1016/j.csr.2007.10.001.

787   Muller, A. A., Ch. J. Reason, V. Mohrholz, M. Schmidt, and A. Eggert, 2014: Computing transport

788   budgets along the shelf and across the shelf edge in the northern Benguela during summer (DJF)

789   and winter (JJA). *J. Mar. Sys.* **140B**, 82-91, doi.org/10.1016/j.jmarsys.2014.02.007.

790   Muller, A. A., V. Mohrholz, and M. Schmidt, 2013: The circulation dynamics associated with a

791   northern Benguela upwelling filament during October 2010. *Continental Shelf Res.* **63**, 59-68.

792   NASA Goddard Space Flight Center, Ocean Ecology Laboratory, Ocean Biology Processing Group.

793   Moderate-resolution Imaging Spectroradiometer (MODIS) Aqua Chlorophyll Data, 2018:

794   Reprocessing. NASA OB. DAAC, Greenbelt, MD, USA. doi:

795   data/10.5067/AQUA/MODIS/L3B/CHL/2018.

796   Nicholson, S. E., 2010: A low-level jet along the Benguela coast, an integral part of the Benguela

797   current ecosystem. *Climatic Change,* **99**, 613–624, doi:10.1007/s10584-009-9678-z.

798   Reynolds, R.W., T. M. Smith, C. Liu, C., D. B. Chelton, K. S. Casey and M. G. Schlax, 2007:

799   Daily high-resolution blended analyses for sea surface temperature. *J. Clim.* **20**, 5473–5496.

800   Pickett, M. H., and J. D. Paduan, 2003: Ekman transport and pumping in the California Current

801   based on the U.S. Navy's high- resolution atmospheric model (COAMPS). *J. Geophys. Res.,*

802   **108**(C10), 3327, doi:10.1029/2003JC001902.

803   Ricciardulli L., and F. J. Wentz, 2016: Remote sensing systems ASCAT C-2015 daily ocean vector

804   winds on 0.25 deg grid, version 02.1. Remote Sensing Systems, Santa Rosa. http://www.remss

805   .com/missi ons/ascat.

806   Rubio, A., B. Blanke, S. Speich, N. Grima, C. Roy, 2009: Mesoscale eddy activity in the southern

807   Benguela upwelling system from satellite altimetry and model data. *Prog. Oceanogr.,* **83**, 288–

808   295.

809   Rykaczewski, R. R., M. David, and J. Checkley, 2008: Influence of ocean winds on the pelagic

810   ecosystem in upwelling regions. *Proceedings of the National Academy of Sciences,* **105** (6), 1965-

811   1970, doi.org/10.1073/pnas.0711777105.

812   Schmidt, M., and A. Eggert, 2016: Oxygen cycling in the northern Benguela Upwelling System:

813   Modelling oxygen sources and sinks. *Progress in Oceanography,* **149**, 145–173,

814   doi.org/10.1016/j.pocean.2016.09.004.

815   Shannon, L.V., 1985. The Benguela ecosystem: evolution of the Benguela, physical features and

816   processes. Oceanogr. *Mar. Biol.* **23**, 105–182.

817   Shannon, L.V., G. Nelson, 1996: The Benguela: Large Scale Features and Processes and System

818   Variability. *The South Atlantic. Springer, Berlin, Heidelberg.* https://doi.org/10.1007/978-3-642-

819   80353-6_9.

820 Small, R. J., E. Curchitser, K. Hedstrom, B. Kauffman, and W. G. Large, 2015: The Benguela

821 upwelling system: Quantifying the sensitivity to resolution and coastal wind representation in a

822 global climate model. *J. Climate*, **28**, 9409–9432, doi:10.1175/JCLI-D-15-0192.1.

823 Thomas A. C., T. P. Strub, R. Weatherbee, and C. Corinne James, 2012: Satellite views of Pacific

824 chlorophyll variability: Comparisons to physical variability, local versus nonlocal influences and

825 links to climate indices. *Deep-Sea Research II*, **77-80**, 99–116,

826 doi.org/10.1016/j.dsr2.2012.04.008.

827 Veitch, J., P. Penven, and F. Shillington, 2010: Modeling Equilibrium Dynamics of the Benguela

828 Current System. *J. Phys. Oceanogr.,* 40(9), 1942-1964.

829 Veitch, J. A., and P. Penven, 2017: The role of the Agulhas in the Benguela Current system: A

830 numerical modeling approach. *J. Geophys. Res*. Oceans, **122**, 3375–3393,

831 doi:10.1002/2016JC012247.

832 Wentz, F.J., J. Scott, R. Hoffman, M. Leidner, A. Atlas, and J. Ardizzone, 2015: Remote Sensing

833 Systems Cross-Calibrated Multi-Platform (CCMP) 6-hourly ocean vector wind analysis product

834 on 0.25 deg grid, Version 2.0. Remote Sensing Systems, Santa Rosa, CA.

835 www.remss.com/measurements/ccmp.

836 Zhaoyun, C., Y. Xiao-hai, J. Young-heon, J. Lide, J. Yuwu, 2012: A study of Benguela upwelling

837 system using different upwelling indices derived from remotely sensed data. *Cont. Shelf Res.*

838 http://dx.doi.org/10.1016/j.csr.2012.05.013.

839

840 Tables

841 Table 1: the explained variability (%) of monthly mean time series of coastal and open-ocean

842 upwelled water off Kunene, Cape Frio, Walvis Bay, Lüderitz, Orange River, Hondeklip Bay, and

843 Cape Columbine by their climatological annual cycle. The explained variability was obtained from

844 the linear regression between the upwelling time series and their climatological annual cycle.

845 sBUS and nBUS are referred to as southern and northern BUS sub-systems, respectively.

Location		Explained variability by climatological monthly mean (%)	
		Coastal upwelled water	Open-ocean upwelled water
nBUS	Kunene	57	14
	Cape Frio	58	23
	Walvis Bay	72	36
	Lüderitz	45	23
sBUS	Orange River	36	44
	Hondeklip Bay	44	16
	Cape Columbine	29	66

846

847   Figure Caption List:

848   Figure 1: Schematic of the mean surface and near-surface flow across the BUS. The blue

849   northward arrows indicate the Benguela Current (BC). The red arrow on the top and bottom

850   represents the Angola Current (AC) and Agulhas Current, respectively. Black arrows display

851   southward undercurrents. Agulhas rings are depicted as red circles. The Angola-Benguela Frontal

852   Zone (ABFZ) separates the BUS from the southward AC. Dash gray contours are the 200m and

853   2000m isobaths.

854   Figure 2: mean state (color shading; m) and variability (contours; m) of the DSL in the model and

855   satellite altimetry data in the 1993-2018 period. To obtain the DSL, the sea surface height

856   averaged over the entire model domain was subtracted in each grid point and time step.

857   Variability is computed from the standard deviation of 5-day averaged values. Rectangular boxes

858   in panel (a) show regions over which areal averaged of the modeled and observed DSL are

859   compared in Fig. S6. Green circles in panel (b) indicate the location of tide gauges utilized to

860   validate the model results in Fig. S5.

861   Figure 3: Long-term mean of ocean vertical velocity (shading; m/day) from the 3-dimension ocean

862   model (a) and the analytical theory (b). The surface wind field is shown (black arrows; m/s), and

863   Chlorophyll-a concentration (dark green contours; mg/m^3). The simulated velocity (a) represents

864   the vertical velocity at the base of mixed layer depth whereas the analytical vertical velocity (b) is

865   estimated from ASCAT wind field records (see Methods). In both panels, Chlorophyll-a

866   concentration is derived from Modis Aqua satellite measurement. The blue contours indicate

867   where the vertical velocity is equal to zero.

42

868   Figure 4: Profiles of the long-term mean Chlorophyll-a concentration (dark-green solid line;

869   mg/m^3), ocean depth (blue solid line; m), simulated (orange dash line; m/day), analytical vertical

870   velocity (orange solid line; m/day; see Methods) and meridional wind velocity (black line; m/s)

871   versus cross-shore distance for seven cross-shore transects. (a), (b), (c), (d), (e), (f), and (g) panels

872   represent the transects in Kunene, Cape Frio, Walvis Bay, Lüderitz, Orange River, Hondeklip Bay,

873   and Cape Columbine, respectively (see Fig.1). Note that the blue vertical line on the right side of

874   each panel represents the first baroclinic Rossby radius of deformation. The simulated velocity

875   (orange dash line) represents the vertical velocity at the base of the mixed layer depth (see

876   Methods). Each variable and corresponding y-axis are shown with identical colors.

877   Figure 5: Variability of simulated (a; m/day) and analytical (b; m/day) water vertical velocity over

878   the 2008-2018 period. In all panels, variability is estimated from the standard deviation (Std) of

879   monthly mean values. Green contours represent the mean of Chl-a concentration (mg/m^3). The

880   simulated vertical velocity is taken at the base of the mixed layer depth.

881   Figure 6: Spatial pattern of the linear correlation coefficients (a) between the simulated and the

882   analytical monthly mean vertical water velocities over the 2008-2018 period. Time series of

883   simulated (thick lines) and analytical (thin lines) coastal (red lines) and offshore (blue lines)

884   upwelled waters across the entire BUS and the northern (26°S-17°S) and the southern (34°S-26°S)

885   BUS subsystems are shown in panel b, c, and d, respectively. The coastal upwelled water is the

886   total upwelled water over the coastal distance of R which is shown by black contour. The offshore

887   upwelled water is the total amount of upwelled water between R and 250km offshore distance.

888   In the top-right corner of panel b-d, the correlation between different time series is displayed.

889   Note that the climatological annual cycle was not subtracted from data. The volume of upwelled
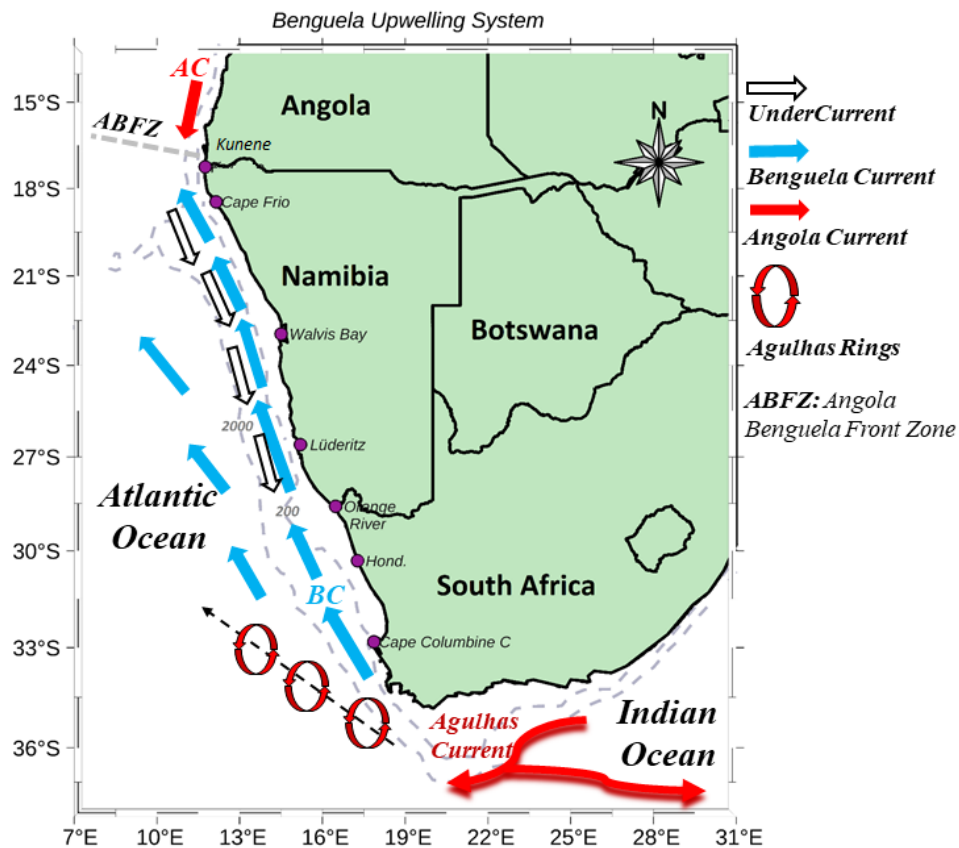
890   water over rectangular boxes in panel (a) is computed and shown in Fig 8-9. Dotted areas in panel

891   (a) show where the correlation is statistically significant at the 95% confidence interval.

892   Figure 7: Spatial pattern of the correlation coefficient between coastal (w_c) and WSCD (w_{curl})

893   upwelling obtained from analytical theory over 2008-2018. Panel (a) represent the correlation

894   between the monthly mean values for all calendar months whereas the panel (b) and (c) show

895   the correlation for November-March and May-September, respectively. In each grid point,

896   shown is the correlation between time series of local WSCD and the coastal upwelling at the

897   same latitude. In all panels, the black contours represent the coastal distance equal to R. Note

898   that in all panels the climatological annual cycle was retained. Dotted areas show where the

899   correlation is statistically significant at 95% confidence interval.

900   Figure 8: Climatological annual cycle (left panels) and time series (right panels) of coastal (thick

901   orange line; $10^6 m^3 s^{-1}$) and offshore (thick blue line; $10^6 m^3 s^{-1}$) amount of upwelled water

902   anomaly computed over coastal and offshore rectangular boxes near Kunene (a,b), Cape Frio

903   (c,d), Walvis Bay (e,f) and Lüderitz (g,h). The rectangular boxes are shown in Fig. 6a. Please note

904   that the y-axis in left panels (a,c,e,g) have different scales. In the right panels, the climatological

905   annual cycle was subtracted in each time series.

906   Figure 9: the same as figure 8 but for Orange River (a,b), Hondeklip Bay (c,d), and Cape

907   Columbine (e,f). Please note that the y-axis in left panels (a,c,e) have different scales.
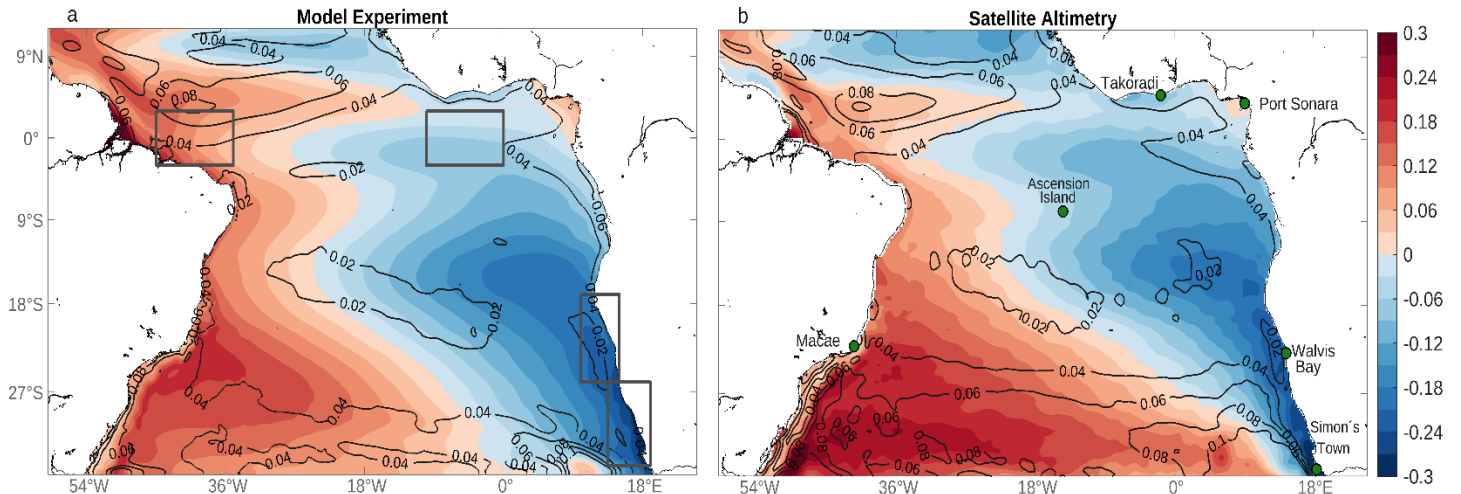
908

909

910

912

Figure 1: Schematic of the mean surface and near-surface flow across the BUS. The blue northward arrows indicate the Benguela Current (BC). The red arrow on the top and bottom represents the Angola Current (AC) and Agulhas Current, respectively. Black arrows display southward undercurrents. Agulhas rings are depicted as red circles. The Angola-Benguela Frontal Zone (ABFZ) separates the BUS from the southward AC. Dash gray contours are the 200m and 2000m isobaths.

919

Figure 2: mean state (color shading; m) and variability (contours; m) of the DSL in the model and satellite altimetry data in the 1993-2018 period. To obtain the DSL, the sea surface height averaged over the entire model domain was subtracted in each grid point and time step. Variability is computed from the standard deviation of 5-day averaged values. Rectangular boxes in panel (a) show regions over which areal averaged of the modeled and observed DSL are compared in Fig. S6. Green circles in panel (b) indicate the location of tide gauges utilized to validate the model results in Fig. S5.

926
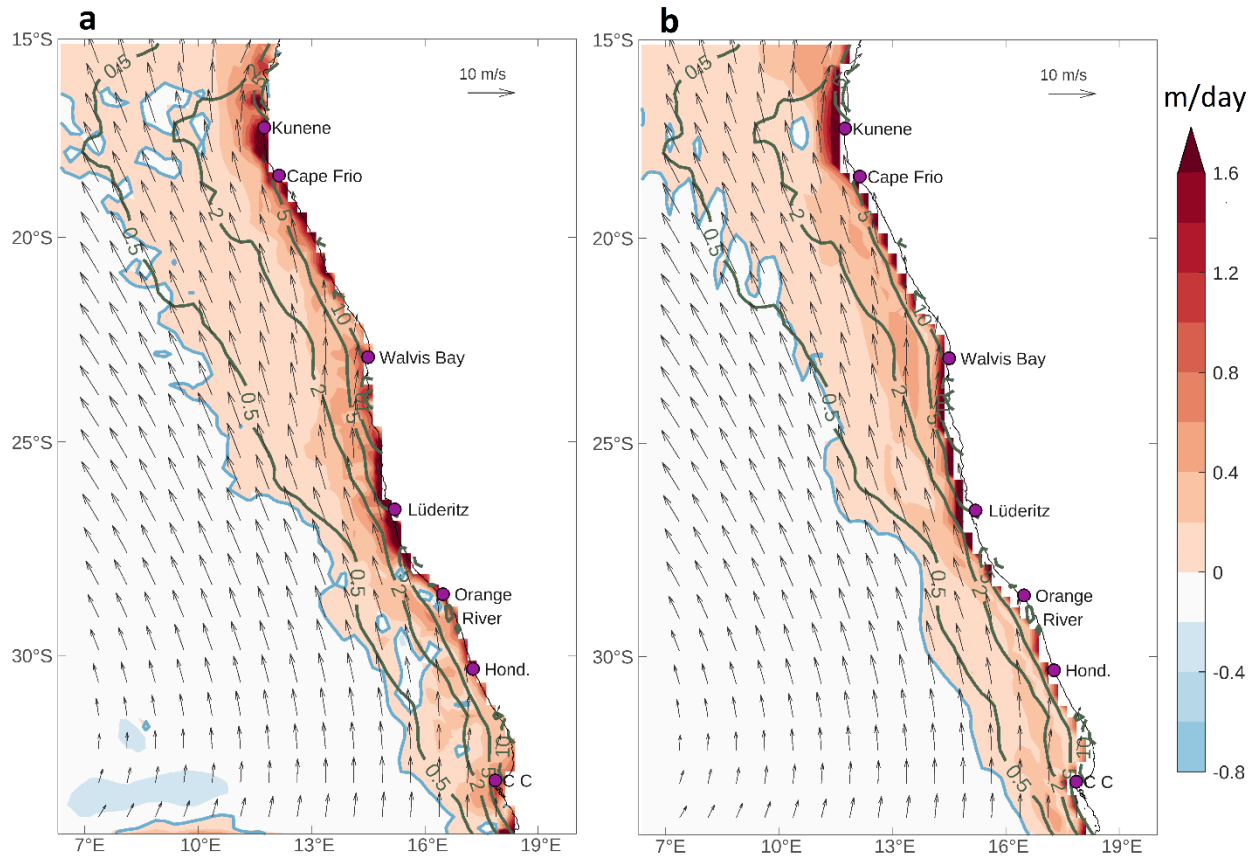
Figure 3: Long-term mean of ocean vertical velocity (shading; m/day) from the 3-dimension ocean model (a) and the analytical theory (b). The surface wind field is shown (black arrows; m/s), and Chlorophyll-a concentration (dark green contours; mg/m^3). The simulated velocity (a) represents the vertical velocity at the base of mixed layer depth whereas the analytical vertical velocity (b) is estimated from ASCAT wind field records (see Methods). In both panels, Chlorophyll-a concentration is derived from Modis Aqua satellite measurement. The blue contours indicate where the vertical velocity is equal to zero.

934
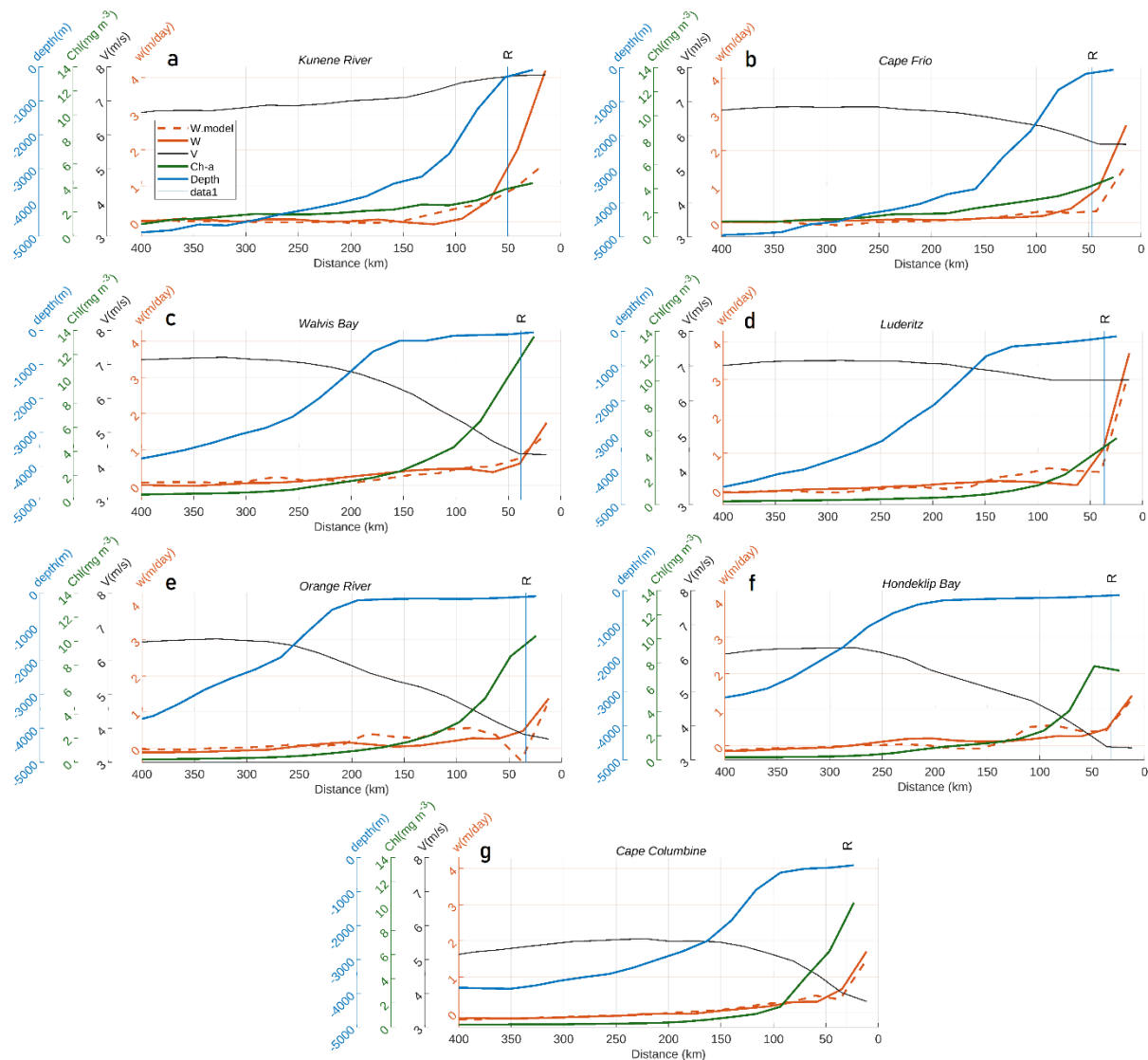
Figure 4: Profiles of the long-term mean Chlorophyll-a concentration (dark-green solid line; mg/m^3), ocean depth (blue solid line; m), simulated (orange dash line; m/day), analytical vertical velocity (orange solid line; m/day; see Methods) and meridional wind velocity (black line; m/s) versus cross-shore distance for seven cross-shore transects. (a), (b), (c), (d), (e), (f), and (g) panels represent the transects in Kunene, Cape Frio, Walvis Bay, Lüderitz, Orange River, Hondeklip Bay, and Cape Columbine, respectively (see Fig.1). Note that the blue vertical line on the right side of each panel represents the first baroclinic Rossby radius of deformation. The simulated velocity (orange dash line) represents the vertical velocity at the base of the mixed layer depth (see Methods). Each variable and corresponding y-axis are shown with identical colors.
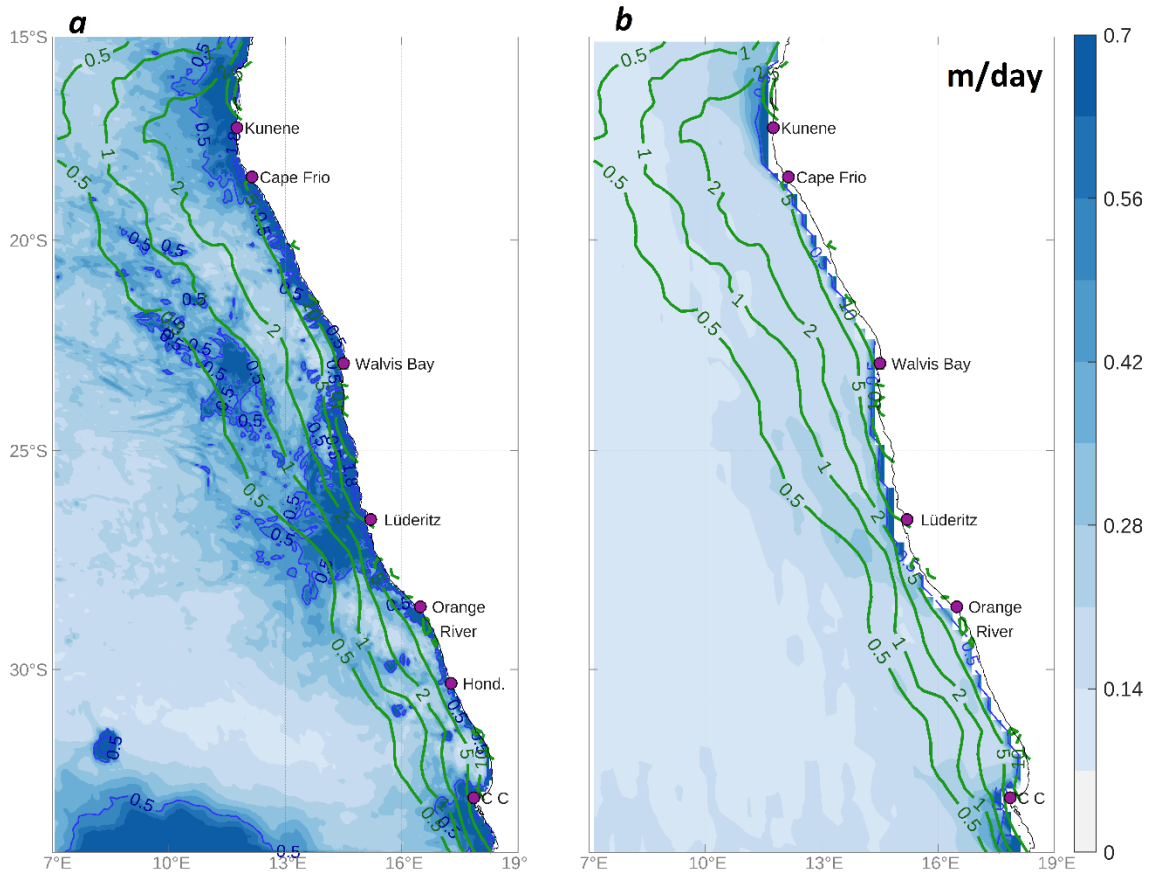
944

Figure 5: Variability of simulated (a; m/day) and analytical (b; m/day) water vertical velocity over the 2008-2018 period. In all panels, variability is estimated from the standard deviation (Std) of monthly mean values. Green contours represent the mean of Chl-a concentration (mg/m^3). The simulated vertical velocity is taken at the base of the mixed layer depth.
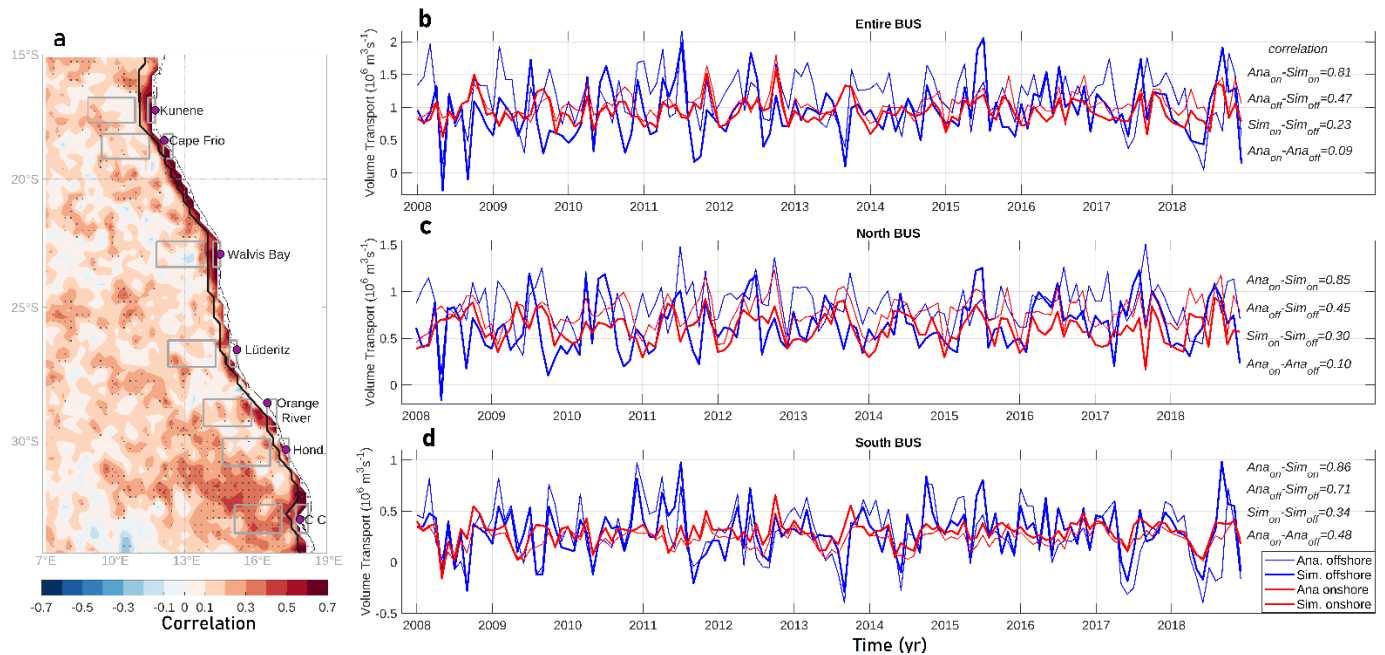
949

Figure 6: Spatial pattern of the linear correlation coefficients (a) between the simulated and the analytical monthly mean vertical water velocities over the 2008-2018 period. Time series of simulated (thick lines) and analytical (thin lines) coastal (red lines) and offshore (blue lines) upwelled waters across the entire BUS and the northern (26°S-17°S) and the southern (34°S-26°S) BUS subsystems are shown in panel b, c, and d, respectively. The coastal upwelled water is the total upwelled water over the coastal distance of R which is shown by black contour. The offshore upwelled water is the total amount of upwelled water between R and 250km offshore distance. In the top-right corner of panel b-d, the correlation between different time series is displayed. Note that the climatological annual cycle was not subtracted from data. The volume of upwelled water over rectangular boxes in panel (a) is computed and shown in Fig 8-9. Dotted areas in panel (a) show where the correlation is statistically significant at the 95% confidence interval.
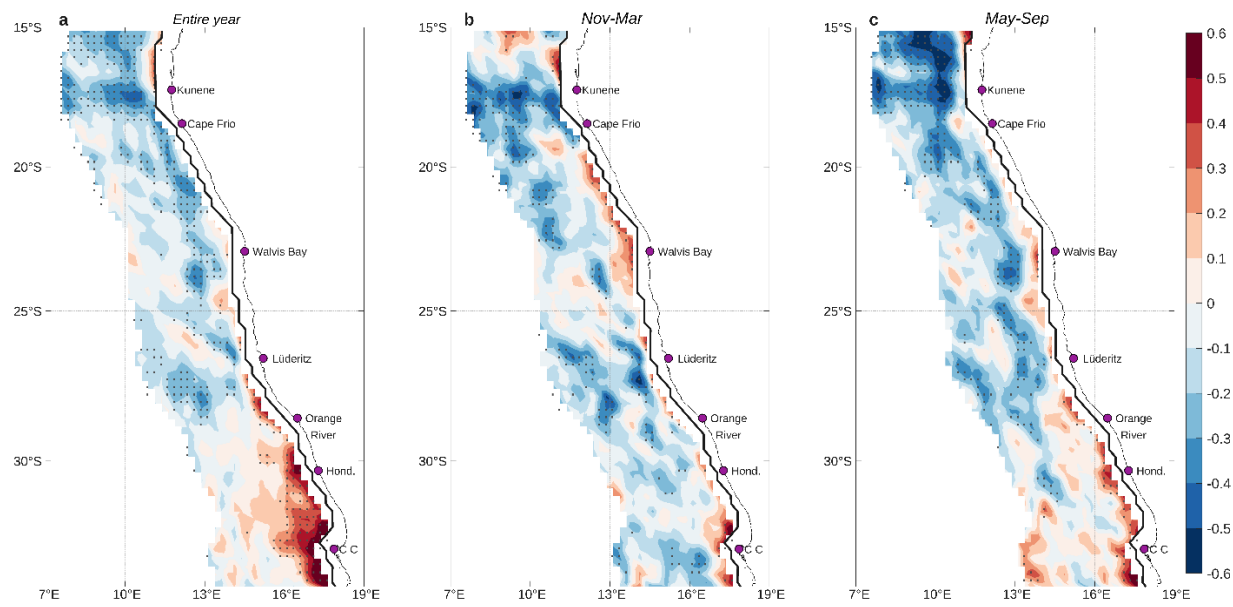
Figure 7: Spatial pattern of the correlation coefficient between coastal (w_c) and WSCD (w_{curl}) upwelling obtained from analytical theory over 2008-2018. Panel (a) represent the correlation between the monthly mean values for all calendar months whereas the panel (b) and (c) show the correlation for November-March and May-September, respectively. In each grid point, shown is the correlation between time series of local WSCD and the coastal upwelling at the same latitude. In all panels, the black contours represent the coastal distance equal to R. Note that in all panels the climatological annual cycle was retained. Dotted areas show where the correlation is statistically significant at 95% confidence interval.
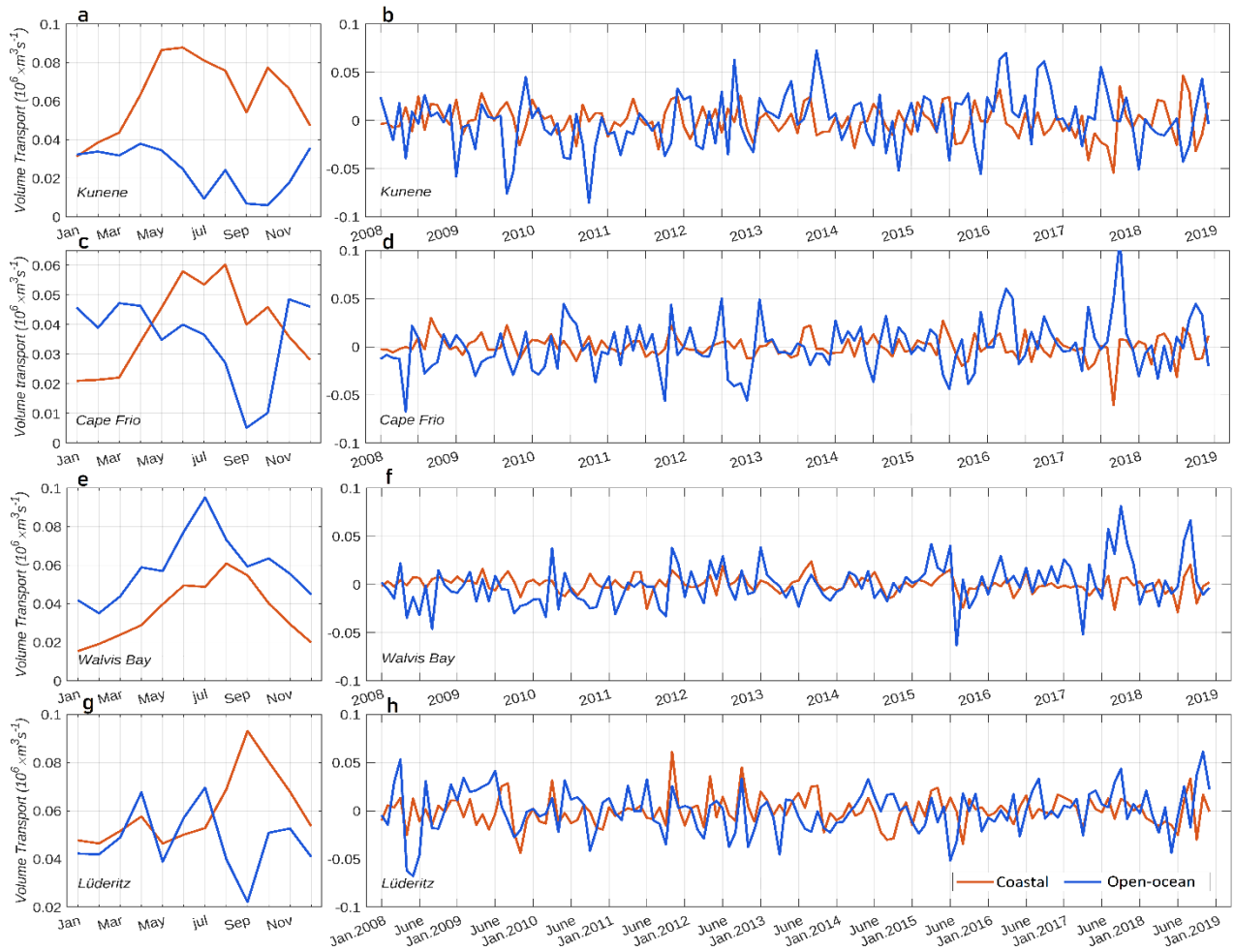
51

Figure 8: Climatological annual cycle (left panels) and time series (right panels) of coastal (thick orange line; $10^6 m^3 s^{-1}$) and offshore (thick blue line; $10^6 m^3 s^{-1}$) amount of upwelled water anomaly computed over coastal and offshore rectangular boxes near Kunene (a,b), Cape Frio (c,d), Walvis Bay (e,f) and Lüderitz (g,h). The rectangular boxes are shown in Fig. 6a. Please note that the y-axis in left panels (a,c,e,g) have different scales. In the right panels, the climatological annual cycle was subtracted in each time series.
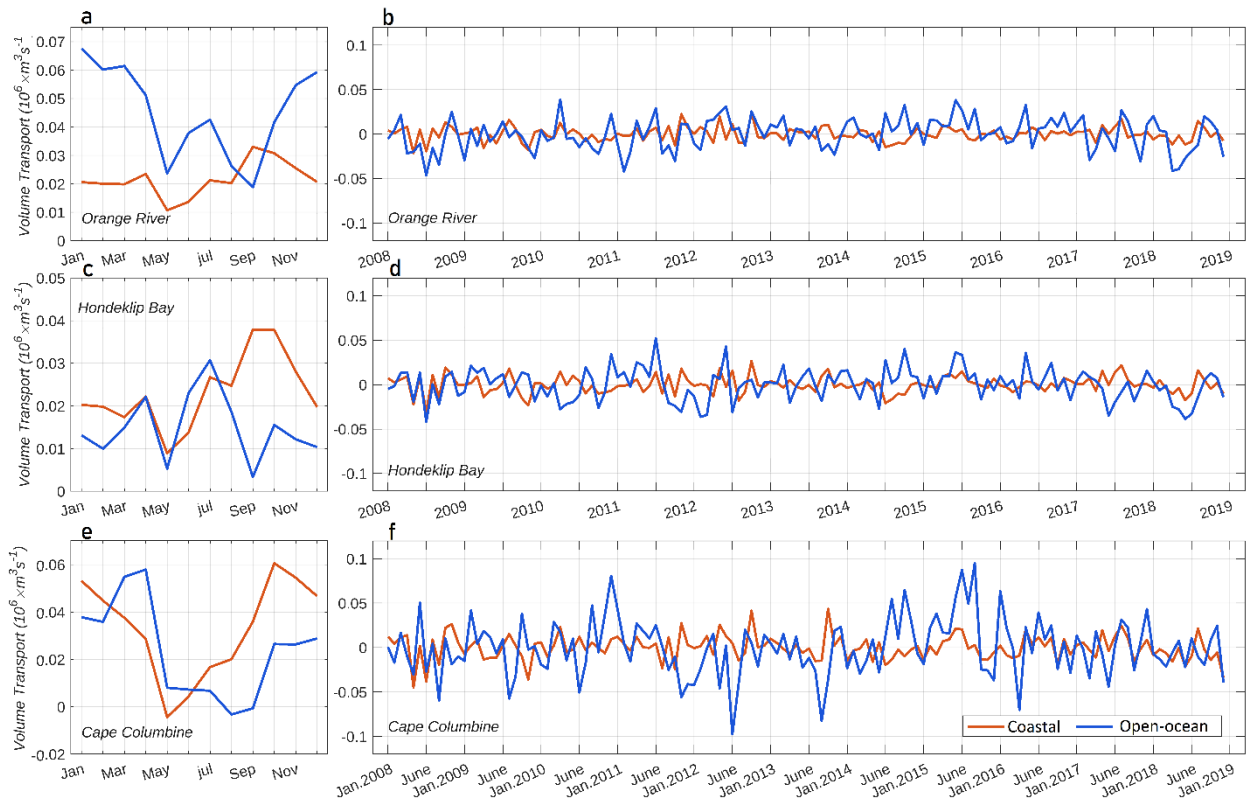
978

979   Figure 9: the same as figure 8 but for Orange River (a,b), Hondeklip Bay (c,d), and Cape

980   Columbine (e,f). Please note that the y-axis in left panels (a,c,e) have different scales.